12-2017

Sinter-Resistant Gold-144 Iron(III) Oxide Core-Shell Structures: Synthesis, Characterization, and Application via Heterogeneous Catalysis

Michelle E. Lukosi
University of Tennessee, mlukosi@vols.utk.edu

To the Graduate Council:

I am submitting herewith a thesis written by Michelle E. Lukosi entitled "Sinter-Resistant Gold-144 Iron(III) Oxide Core-Shell Structures: Synthesis, Characterization, and Application via Heterogeneous Catalysis." I have examined the final electronic copy of this thesis for form and content and recommend that it be accepted in partial fulfillment of the requirements for the degree of Master of Science, with a major in Chemistry.

Sheng Dai, Major Professor

We have read this thesis and recommend its acceptance:

Craig E. Barnes, Ampofo K. Darko, Siris O. Laursen

Accepted for the Council:
Dixie L. Thompson

Vice Provost and Dean of the Graduate School

(Original signatures are on file with official student records.)

Sinter-Resistant Gold-144 Iron(III) Oxide Core-Shell Structures:
Synthesis, Characterization, and Application via Heterogeneous Catalysis

A Thesis Presented for the
Master of Science
Degree
The University of Tennessee, Knoxville

Michelle E. Lukosi
December 2017

DEDICATION

I owe all my success to my loving family:

My husband, Eric, and my children, Aria and Ian, for always giving me the opportunity to live, laugh, and love life.

ACKNOWLEDGEMENTS

I want to thank my advisor, Dr. Sheng Dai, for his support and encouragement throughout my graduate career. To Chengcheng Tian and Huiyuan Zhu, for being so patient with my many questions. To Nada Mehio, for always being so positive and uplifting. To Jennifer Schott, KC Mote and all of my other colleagues, thank you for tolerating my quirky moods.

Thank you to my awesome mother, Jeana Ismert, for letting me call her all the time and talk about subject matter she didn't understand, but let me prattle on anyway. Thank you to my loving husband, Eric Lukosi, for his support, patience, guidance, and faith in me through this entire process; without his confidence in me, I know I would not be where I am today. And lastly, but certainly not least, a special thanks to my wonderful children, Aria and Ian, who always remind me not to be too serious, but instead to be silly, have fun, and to stay balanced! I would not have been able to do this without my family, nor would I have had it any other way.

ABSTRACT

In the realm of catalysis, small nanoparticles have been an area of interest due to their high surface-to-volume ratio. This is even more so with gold nanoparticles in that gold only becomes catalytically active with small particles sizes. Thus, gold clusters are desirable given their uniformity, high surface-to-volume ratio, and high catalytic activity. Given the nature of small gold particles to sinter, it was found to be advantageous to protect the particles using a gold-metal oxide core-shell configuration. Core-shell heterostructures have been utilized as a catalyst that is thermally stable and exhibits a synergistic effect between core and shell, resulting in increased catalytic activity. The research contained in this document discusses the synthetic procedure of a gold-144 cluster using a variation of the Brust-Schiffrin method followed by an iron oxide coating via post-selective oxidative treatment to create a gold-144 iron oxide core-shell structure. Shell thickness is varied depending on the amount of iron precursor used and studied under the particle's catalytic efficiency with carbon monoxide oxidation. The gold-144 iron oxide particles with Au:Fe mass ratios of 1:2, 1:4, and 1:6 were synthesized and then deposited onto silica via colloidal deposition. Using CO oxidation, each gold-144 iron oxide catalyst loaded onto silica gave varying degrees of full CO conversion depending on the thickness of the iron oxide layer. The 1:4 gold-144 iron oxide catalyst produced the best catalytic activity and was further investigated using 2-propanol conversion as well as thermal treatments using CO oxidation. Under CO oxidation, the 1:4 structure calcined at 300 degrees Celsius presented the best results, and the 1:4 ratio was still active at 100 degrees Celsius after thermal treatments. Under 2-propanol conversions, the data seems to suggest that core-shell structure provides a synergistic effect for acetone production, however, this cannot be concluded until further testing is accomplished.

TABLE OF CONTENTS

Chapter One Introduction and general information 1
Catalysis 1
Kinetic Models 2
Gold in Catalysis 3
Chapter Two Literature Review 6
Gold Nanoparticles 6
Gold Clusters 6
Core-Shell Particles 8
Core-Shell Syntheses 12
Seed-mediated Growth 12
Post Selective Oxidation Treatment 21
One-Pot Chemical Synthesis 24
Au-Metal Oxide Core-Shell Structures: CO Oxidation 26
Shell Thickness on Catalytic Activity 26
Core Size on Catalytic Activity 27
Core-Shell Interfacial Synergies 29
Core-Shell vs. Non-encapsulated Catalyst Counterparts 29
Chapter Three Materials and Methods 31
Materials 31
Catalyst Preparations 31
Characterizations 33
X-ray Diffraction 33
Matrix Assisted Laser Desorption Ionization 34
Brunauer-Emmett-Teller Analyzer 36
Inductively Coupled Plasma Optical Emission Spectroscopy 36
Scanning Transmission Electron Microscopy 38
X-ray Photoelectron Spectroscopy 39

Fourier-Transform Infrared Radiation 39
Characterization of Catalytic Activity 40
Chapter Four Results and Discussion 42
$Au_{144}(SC_6H_{13})_{60}$ Nanocluster 42
$Au_{144}@Fe_2O_3$ Core-Shell Structure 42
Varied Shell Thickness 42
Synergistic effects of core-shell system 50
CO Oxidation 50
2-Propanol Conversion 52
Thermal Treatments of 1:4 $Au_{144}@Fe_2O_3/SiO_2$ Structure 53
Chapter Five Research Conclusions 58
$Au_{144}@Fe_2O_3$ Core-Shell Structure 58
Future Directions 58
References 60
Appendix 69
Vita 76

LIST OF TABLES

Table 1. Metal Oxide Bulk Applications.....11
Table 2. BET surface area and ICP-OES weight percent of core-shell structure loaded onto silica. 45
Table 3. XPS – Surface Composition (at.%): Au_{144}@Fe_2O_3/SiO_2.....50
Table 4. 2-Propanol conversion activation energies (E_{act}). 53

LIST OF FIGURES

Figure 1. Simple exothermic potential energy diagram. 1
Figure 2. A) Langmuir-Hinshelwood, B) Eley-Rideal, & C) Mars van Krevelen mechanisms. Figure modified from reference.[7] 3
Figure 3. Possible pathways for CO oxidation over supported gold. Figure modified from reference.[19] 5
Figure 4. Three different synthetic pathways for Au-metal oxide core-shell structures.[20] 9
Figure 5. A) SEM image and B) TEM image of Au@Cu_2O core-shell NPs with the shell thickness about 20 nm. Figure modified from reference.[76] 14
Figure 6. HAADF-STEM image of AuNR@Cu_2O heterostructure. Figure modified from reference.[65] 14
Figure 7. Different Au core nanoparticle structures (top) forming different Cu_2O shell configurations (bottom) with a scale bar = 100 nm. Figure modified from reference.[78] 14
Figure 8. TEM images of A) 5 nm Au NPs, B) dumbbell-like Au-Fe_3O_4 heterostructures, D) 10 nm Au NPs, and E) flower-like Au-Fe_3O_4 heterostructures; C) and F) are high-resolution transmission electron microscopy (HRTEM) images of dumbbell- and flower-like Au-Fe_3O_4 heterostructures, respectively. Figure modified from reference.[39] 16
Figure 9. The Au−ligand−ZnO and the Au−ligand−PVP−ZnO interactions in Au@ZnO heterostructures. Figure modified from reference.[70] 17
Figure 10. Fabrication of the AuNR@Ag@mSiO_2 core-shell structures. Figure modified from reference.[80] 18
Figure 11. Fabrication process of Au@ZrO_2 yolk-shell structure and TEM images at each stage. Figure modified from reference.[92] 21
Figure 12. A) STEM-EELS 2D mapping of C-$Au_{44}Mn_{56}$ after annealing and B) synthesis of Au-MnO heterostructures. Figure modified from reference.[44] .. 23

Figure 13. A) Synthesis of Au@CeO_2 core-shell structures and B) HAADF-STEM mapping image of one Au@CeO_2 heterostructure. Figure modified from reference.[75] 23
Figure 14. A) Synthesis of Au@TiO_2 core-shell heterostructure using reverse micelle method B) TEM and C) elemental mapping of Au@TiO_2 core-shell heterostructure. Figure modified from reference.[95] 25
Figure 15. A) Diagram of the gas bubbling-assisted membrane reduction-precipitation (GBMR/P) device for synthesis of ZrO_2-supported Au@CeO_2 core-shell heterostructure B) one-pot synthesis of Au@CeO_2/ZrO_2 using the GBMR/P method. Figure modified from reference.[47] 25
Figure 16. CO conversion vs. temperature by Au@SiO_2 heterostructures of varying gold core sizes. Figure modified from reference.[67] 28
Figure 17. Conversion temperature curves for CO oxidation (a-d: Au core of 14 nm). A) Au@ZrO_2, B) Au@ZrO_2,C, C) Au@C silica route, D) Au@C zirconia route, E) Au@C zirconia route (Au core of 7 nm). Figure modified from reference.[62] 30
Figure 18. CO conversion using A) Au@SnO_2 core-shell structure and B) non-encapsulated Au/SnO_2 catalysts. Figure modified from reference.[61] 30
Figure 19. Seed-mediated post-selective oxidation method for Au_{144}@Fe_2O_3 particles. 32
Figure 20. Simplistic laser desorption ion source for non-resonant light absorption by a solid. Figure modified from reference.[101] 35
Figure 21. MALDI matrix trans-2-[3-(4-tert-butylphenyl)-2-methyl-2-propenylidene] malononitrile (DCTB). 37
Figure 22. Typical isotherm for N_2 adsorption-desorption, originally from Macken, 1996. Figure modified from reference.[107] 37
Figure 23. MALDI-TOF-MS of $Au_{144}(SC_6H_{13})_{60}$ with peak at 32,500 m/z (Da) A) experimental results vs B) literature results. Figure modified from reference[27] 43

Figure 24. XRD of $Au_{144}(SC_6H_{13})_{60}$ thin film with broad peak at 38.58° 2θ indicative of small Au domain. 43
Figure 25. A) HAADF-STEM of 1:4 $Au_{144}@Fe_2O_3$ structure as synthesized, as well as the B) Fe (blue) and C) O (red) areal density of the structure. 46
Figure 26. STEM of $Au_{144}@Fe_2O_3/SiO_2$ with varying Fe_2O_3 content for the A) 1:2, B) 1:4, and C) 1:6 structures. 47
Figure 27. XRD of $Au_{144}@Fe_2O_3/SiO_2$ with varying Fe_2O_3 content for A) 1:2, B) 1:4, and C) 1:6 structures, with a line at 38.2° 2θ where bulk gold peaks are prominent. 48
Figure 28. XPS of surface composition of $Au_{144}@Fe_2O_3/SiO_2$ 1:4 structure showing A) the survey spectrum and the high-resolution spectra of B) gold, C) iron, D) oxygen, E) silicon, and F) carbon. 49
Figure 29. CO conversion on $Au_{144}@Fe_2O_3/SiO_2$ catalysts with varying Fe_2O_3 shell thickness, as well as Au_{144}/SiO_2 and Fe_2O_3/SiO_2. 51
Figure 30. FTIR of CO adsorption onto 1:4 structure $Au_{144}@Fe_2O_3/SiO_2$ at 5 °C (gaseous CO contribution subtracted). 53
Figure 31. 2-Propanol conversion reactions showing A) 2-propanol consumption rates, B) acetone production rates, and C) propene production rates. 55
Figure 32. 2-Propanol conversion reactions showing selectivity to A) propene, B) acetone, and C) of an unknown compound. 56
Figure 33. The 1:4 $Au_{144}@Fe_2O_3/SiO_2$ structure calcined at temperatures 300, 500 & 700 °C showing A) CO conversion and B) XRD spectra. 57
Figure A1. A, B, & C) HAADF-STEM of $Au_{144}@Fe_2O_3$ 1:4 structure, pre-calcined. 70
Figure A2. A & B) STEM of $Au_{144}@Fe_2O_3/SiO_2$ 1:2 structure, calcined at 300 °C. 71
Figure A3. A-D) STEM of $Au_{144}@Fe_2O_3/SiO_2$ 1:4 structure, calcined at 300 °C. 71
Figure A4. A-D) STEM of $Au_{144}@Fe_2O_3/SiO_2$ 1:6 structure, calcined at 300 °C. 72
Figure A5. Isotherm for adsorption-desorption of N_2 at 77 K on fumed silica (SiO_2). 73

Figure A6. Isotherm for adsorption-desorption of N_2 at 77 K on Fe_2O_3/SiO_2 with 2.3% Fe loading. 73
Figure A7. Isotherm for adsorption-desorption of N_2 at 77 K on Au_{144}/SiO_2 with 1.4% Au loading. 74
Figure A8. Isotherm for adsorption-desorption of N_2 at 77 K on 1:2 Au:Fe by mass $Au_{144}@Fe_2O_3/SiO_2$ with 1.2% Au loading. 74
Figure A9. Isotherm for adsorption-desorption of N_2 at 77 K on 1:4 Au:Fe by mass $Au_{144}@Fe_2O_3/SiO_2$ with 1.7% Au loading. 75
Figure A10. Isotherm for adsorption-desorption of N_2 at 77 K on 1:6 Au:Fe by mass $Au_{144}@Fe_2O_3/SiO_2$ with 1.5% Au loading. 75

CHAPTER ONE

INTRODUCTION AND GENERAL INFORMATION

Catalysis

The word itself comes from the Greek roots *cata-* and *-lysis*, meaning 'a breaking down' and can be can be related by the breaking down of chemical barriers for a reaction.[1] In 1794, the concept was first described in a book, by Elizabeth Fulhame, entitled An Essay on Combustion, where water was deemed a catalyst for oxidation-reduction reactions, in that it was required for the reaction to proceed, but was not consumed.[2-3] The term is later coined by the scientist Jacob Berzelius in 1836,[4] where he explains that "[c]atalytic power means that substances are able to awake affinities that are asleep at [said] temperature by their mere presence."[5]

Catalysis is a process in which a catalyst is a substance that increases the reaction rate by lowering the activation energy of a chemical process, without being consumed, in that it is both a reactant and a product (Figure 1). Further, catalysis can be categorized into two basic categories, homogeneous and heterogeneous

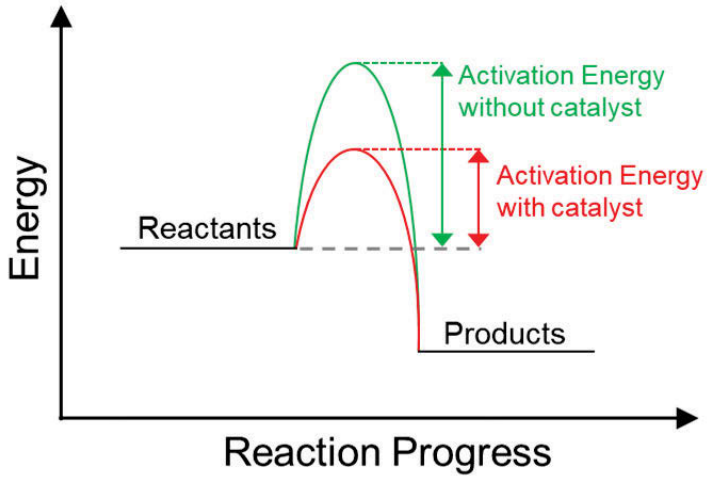

Figure 1. Simple exothermic potential energy diagram.

catalysis. Homogeneous catalysis involves a one-phase system, where the catalyst and other reactants are in the same phase as one another, such as liquid or gas phase. Heterogeneous catalysis is a two-phase system, where the catalyst is typically in the solid phase, while the other reactants are in the gas or liquid phase. The reaction itself then occurs at the interface between the two phases.

Kinetic Models

There are three basic kinetic models for catalytically active surfaces: the Langmuir-Hinshelwood, the Eley-Rideal, and the Mars van Krevelen mechanisms (Figure 2). In the first mechanism, the Langmuir-Hinshelwood mechanism involves a partial polarization of gold (Au) atoms within the particle. In this mechanism, both reactants adsorb (or chemisorb) onto the surface. For carbon monoxide (CO) oxidation, molecular oxygen (O_2) is activated when the O-O bond is stretched by electron transfer from Au.[5] After which, surface diffusion facilitates interaction between the adsorbed molecules for a bimolecular reaction. Then, the product desorbs from the surface. The reaction at the surface, for this mechanism, is typically the rate limiting step, as shown below, in mechanism (1).

$$\begin{aligned} &CO(g) \rightleftharpoons CO(ads) \\ &O_2(g) \rightleftharpoons 2O(ads) \\ &CO(ads) + O(ads) \xrightarrow{rds} CO_2(ads) \xrightarrow{fast} CO_2(g) \end{aligned} \qquad (1)$$

In the second mechanism, the Eley-Rideal mechanism, one reactant adsorbs onto the surface, while the other reactant, still in the gas or liquid phase, interacts directly with the adsorbed species. This is followed by desorption of the reaction product. For CO oxidation on Au, CO would adsorb onto the surface, interact with half of an oxygen molecule, and then desorb as carbon dioxide (CO_2). This mechanism is not as likely as the Langmuir-Hinshelwood mechanism because the oxygen would need to be activated in order to react with the chemisorbed CO. However, there has been some evidence that it is able to occur under certain circumstances.[6] Under the third mechanism, the Mars van Krevelen mechanism applies to oxidations catalyzed by easily reducible oxides that will be able to

release lattice oxide ions in order to oxidize the other reactant. The CO adsorbs onto the catalyst surface, an adjacent lattice oxygen is essentially released to interact with the adsorbed CO, and, then, CO_2 is desorbed from the surface. The released lattice oxide ion creates a vacancy, which is then replaced by an O_2^- anion or the dissociation of molecular oxygen.

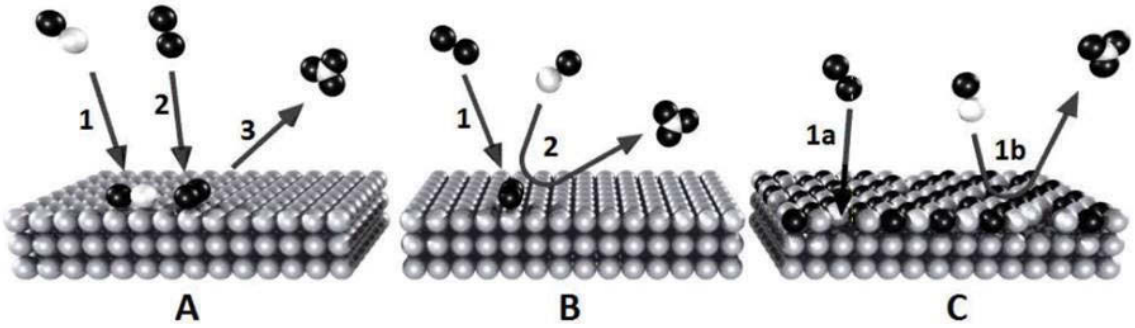

Figure 2. A) Langmuir-Hinshelwood, B) Eley-Rideal, & C) Mars van Krevelen mechanisms. Figure modified from reference.[7]

Gold in Catalysis

Gold was discovered as a viable catalyst in the 1980's by Masatake Haruta, who found that it is an excellent catalyst for CO oxidation at low temperatures.[8] Based on these findings, gold has since been extensively investigated as a catalyst. An advantage of gold over many other noble metals is that humidity does not seem to depress its catalytic activity, but can actually enhance it.[9] Subsequently, gold was discovered to only be catalytically active as small nanoparticles, showing optimal catalytic activity in the range of 0.5-5.0 nm in diameter,[10-12] as opposed to larger particles or bulk gold. In addition, it has also been predicted that, when gold NPs are below 3.5 nm (< 300 atoms), there is a metal-to-nonmetal transition that occurs for gold NPs where they become insulators.[13] The observed change in electrical conductivity is due to quantum

confinement of electrons,[14] where the NPs are near the size to that of the de Broglie wavelength of upper level electrons that are responsible for conduction.

Catalytic reactions take place at the surface of the catalyst, and therefore, the larger the surface-to-volume ratio, the more catalytic sites that are available per volume. For this reason, NP/NC catalysts are synthesized with the thought of the smaller the better in order to increase surface-to-volume area and augment catalytic activity. However, gold catalysts smaller than 2 nm are less stable[15] and have not been as highly researched as their larger nanomaterial counterparts. In general, gold NPs are difficult to characterize because they cannot be fully elucidated under a single catalytic platform.[16] In addition to multiple characterization methods there are also a few different kinetic mechanisms that are typically discussed for Au catalyzed reactions.

For supported gold, this means that the support surface is playing an active role in the catalysis process. The mechanisms may vary from one type of catalyst to another. More than one mechanisms may be operating on the catalyst at the same time and mechanisms may be dependent on a given set of reaction conditions, such as temperature, humidity and partial pressures. Mechanisms may be broken up into four basic categories: involving only metallic gold, requiring simultaneous availability of metallic gold and cationic gold, collaboration between metal and support (a Mars van Krevelen type reaction), and proceeding with cationic species on the support (Figure 3).[5]

In catalysis mechanisms that involve only the gold component, the gold must be fully reduced (Au^0) to be catalytically active. Reducing gold typically requires thermal activation. By themselves, cationic gold species (Au^{1+} and Au^{3+} being the most common) are inactive, but can become catalytically active when in combination with Au^0. Cationic Au may be either located at the interface between the metal and support[17] or atomically dispersed in or on the support.[18] Before moving on, a thorough review of gold nanoparticles, gold nanoclusters, and their applications in core-shell structures need to be looked at in-depth.

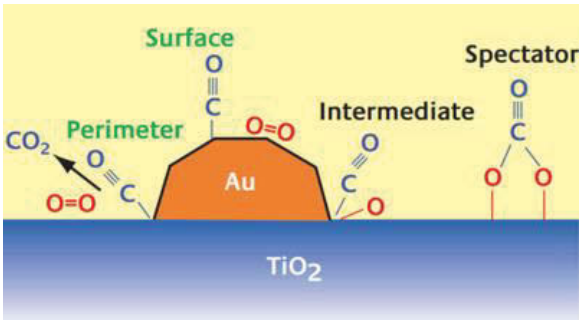

Figure 3. Possible pathways for CO oxidation over supported gold. Figure modified from reference.[19]

CHAPTER TWO

LITERATURE REVIEW

Part of the information in this chapter is taken with permission from Michelle Lukosi's paper.[20]

Gold Nanoparticles

Due to their small size, gold nanoparticles are prone to sintering and aggregation, which reduces their catalytic activity and long-term stability for catalytic processes. Coalescence of gold nanoparticles has been predicted to occur via surface diffusion, which is curvature dependent, while taking into account the energy released due to surface reduction. In turn, the energy that is released will increase temperatures, and accelerate the sintering process.[21] Bulk gold has a melting point of 1300 °C, but it's Tammann temperature is at 395 °C.[22] This is the temperature for which the mobility of the metal becomes measurable. For very small particles, this is the temperature at which they will sinter when in close proximity to one another. Using a core-shell framework is one such way that has been developed to protect the catalyst and prevent sintering, so that a plausible number of active sites are maintained.

Gold Clusters

As research into catalytic gold emerged, so did research into uniform catalysts that could deliver consistent and reproducible results. This opened the door to nanocluster catalysis. Thiolate-protected gold nanoparticles, first proposed by Brust and Schiffrin,[23] has become the building block to obtaining a well-defined $Au_n(SR)_m$ formula using specific Au-to-thiol ratios. Here, the cluster with a number of gold atoms, n, corresponds to a certain number of thiolate groups, m, encompassing a sulphur atom (S) and an organic rest group (R), which creates a monolayer surrounding the gold cluster.[24-25]

To be clear, the only real distinction between nanoclusters and nanoparticles is that the term cluster is used when referring to a system of known chemical composition and structure, whereas the term nanoparticle is used when a system is less precise and instead identified within a certain size distribution.[26] Understanding how to synthesize NCs with exact composition is desirable in creating a uniform product that will make it easier to reproduce findings, results, and to understand what catalytic properties can be associated with certain dimensions and morphologies.

The Au_{144} nanocluster has been recognized as one of the larger, relatively stable, gold clusters.[27-31] Its structure has been established experimentally, utilizing techniques such as electrospray ionization (ESI), matrix assisted laser desorption ionization mass spectrometry (MALDI-MS), scanning transmission electron microscopy (STEM), and X-ray spectroscopy.[29, 32-34] Weissker *et al.* performed time-dependent density-functional theory (TD-DFT) calculations that show individual peaks representing discrete levels of the structures localized electronic states.[35] This means there is a discrete energy band structure that develops for small clusters, hence there is a metal-to-nonmetal transition, similar to that of semiconductors.[14] That being stated, gold nanoparticles by themselves tend to sinter easily, losing their catalytic ability. The smaller the particles, the more this sintering becomes a prominent issue. This is, in large part, why very small gold nanoparticles and clusters are difficult catalysts to effectively utilize. To stabilize gold nanoparticles, at the very least, they are loaded onto a support. The support is generally a metal oxide,[36] but others have reported using other support types, such as carbon-based or titanium(IV) chloride supports.[37-38] Even with different support structures, small Au nanoparticles, <10 nm in diameter, tend to sinter above room temperature.

In the interest of overcoming this issue, core-shell structures have been investigated,[39-47] where the gold nanoparticle is the core with a protective, often metal oxide, shell. This allows the gold to retain its size and shape, which

preserves its catalytic ability under thermal and mechanical stress. These core-shell structures have not yet been investigated for small gold clusters, due to the cluster's delicate nature. Given the large increase in surface-to-volume ratio for cluster-sized core-shell structures, they are a potential effective catalyst, exhibiting more catalytic sites compared to larger particles of the same volume. For this reason, research into their stabilization is key.

Core-Shell Particles

There are several benefits for catalysts utilizing the core-shell design. In this catalyst formation, a thermally stable shell, in theory, protects the catalytic noble metal core when exposed to elevated temperatures, which allows the core to retain its crystal size and structure.[42] Secondly, they can retain their catalytic properties after repeated cycles due to the configuration's stability. Thirdly, when properly designed, the core-shell structure can enhance the catalytic performance of the nanostructure due to the synergistic effects between the core and shell.[48-49]

In the core-shell morphology, the shell is typically a metal oxide that can act as an electron transfer agent and also provide strong metal support interaction (SMSI). SMSI refers to the robust interaction that can occur between a catalytic metal (e.g. gold) and the oxide support, or shell in this case. Different metal oxide supports have been shown to provide different SMSIs, which have the ability to create these contact zones with enhanced catalytic properties for certain reactions.[50] For this reason, the metal oxide support should consider shell porosity, magnetic behavior, electronic properties, thermal stability, crystalline structure and, ultimately, how it fits with the specific needs of the application. Just as gold behaves differently on the nanometer scale, so do many other elements, for which a comprehensive study on such behaviors and the possible combinations is complicated. Furthermore, there are differing views on whether the site of catalysis happens at the surface of the noble metal core, between the core and shell matrices, or on the shell itself, which would make a study of direct core and shell

combinations all the more important in how they would either enhance or dampen catalytic activity.

There are many different ways to synthesize core-shell structures, but they can be separated into three basic categories: seed-mediated growth, post selective oxidative treatment, and one-pot chemical synthesis (Figure 4). Seed-mediated growth is the process where the noble metal core, or seed, is synthesized first and then followed by epitaxial growth of the metal oxide shell onto the noble metal. One-pot synthesis is the simultaneous formation of the noble metal core and metal oxide shell. One-pot synthesis is attractive for its ease and simplicity, but makes it quite difficult to fine-tune the core and shell dimensions and structure. Post selective oxidation is usually applied to a bimetallic system, or alloy, and upon heating the component that is more easily oxidized will be drawn out, typically leaving a noble metal core with a metal oxide shell. However, this method can also be quite difficult to control the morphologies of the core-shell structure.

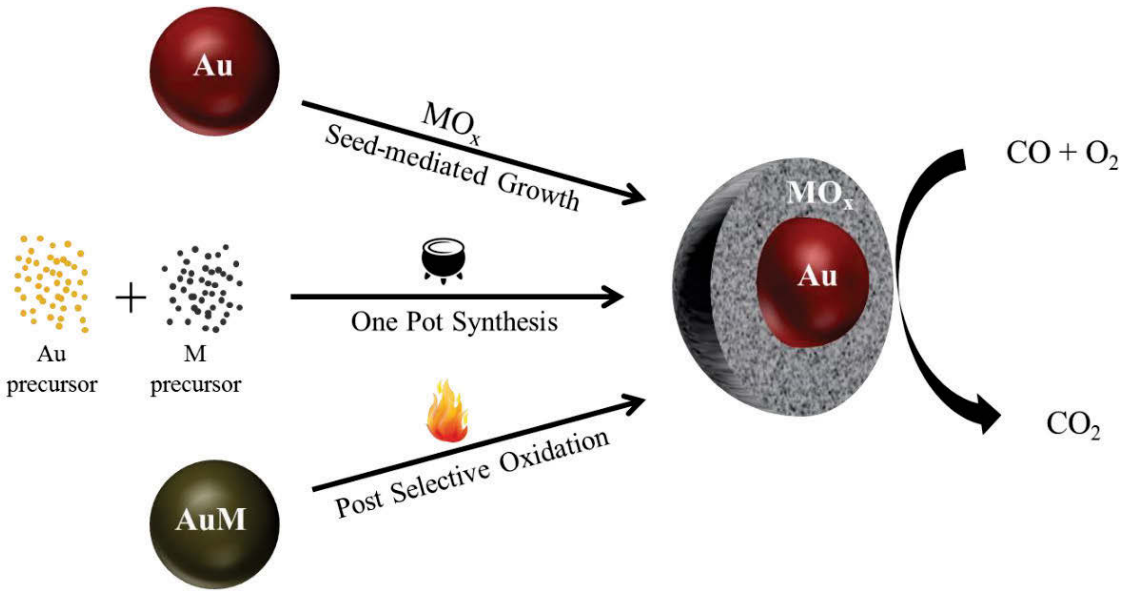

Figure 4. Three different synthetic pathways for Au-metal oxide core-shell structures.[20]

Typically, when discussing core-shell structures it is represented by NM@MO_x, where the noble metal, NM, core is fully encapsulated, @, by a metal oxide, MO_x, and a non-encapsulated structure is mostly represented by NM/MO_x notation, where the noble metal is on top of a metal oxide support.

Of the synthetic methods, there are many different metal oxides than can be used as a shell. Different noble metals act differently from one another with the same metal oxide shell, and exhaustive experimental research has sought the optimum combination of core and shell for various catalytic processes. This non-exhaustive list of potential metal oxides (Table 1) exhibits different properties in the catalytic process. It should be noted that the given band gap energies listed in Table 1 are those that have been observed for bulk metal oxides. However, non-oxygen containing semiconductors have also been investigated, such as the monocrystalline cadmium selenide (CdSe) shell.[51] Due to quantum confinement of electrons in a nanoparticle, the bandgap can shift to a higher energy when the radius of the particle is decreased to a size where the free electron wavelength (calculated using de Broglie's equation) in a semiconductor is on the order of the size of the nanoparticle.[52-53] This can be visualized by realizing that the number of electrons, and therefore available states, within the system are not sufficient to create the "bands" of a bulk material. For small particles, the available states resemble a bandgap, but the separation is larger than that in a bulk material.

In the case of a core-shell structure, the situation becomes more complicated. The core-shell structure is essentially a heterostructure, between the core and the shell. The interface between the two regions of the heterostructure will define how electron transfer across the shell can take place to enable efficient catalysis. The shell is typically much larger than the core, but even in the case of a monolayer-thick shell, as long as the shell particles are periodically bonded together in a regular crystalline structure, the electrons are only confined in one dimension, complicating the analysis. The challenge of understanding the electron transport in the core-shell structure is further complicated by the existence of defects, such as Frenkels and interstitials, which alter the delicate electronic

Table 1. Metal Oxide Bulk Applications.

Metal Oxide	Chemical Formula	Band Gap (eV)	Significant Findings	Reference
Zinc Oxide	ZnO	3.3	Investigated for methanol steam reforming	54-55
Titania	TiO_2	3.2	High rate of electron-hole recombination and thermal stability	49, 56-57
Tin(IV) Oxide	SnO_2	3.6	Application in gas sensors (high sensitivity, low operating temperatures); n-type semiconductor	58-61
Zirconia	ZrO_2	5.0	Hydrophobic; crystal structures: monoclinic, cubic, and tetragonal	62-64
Ceria	CeO_2	3.8	Used for diesel soot combustion	47
Cuprous Oxide	Cu_2O	2.2	Large light absorption coefficient and good photocatalytic activity; p-type semiconductor	65
Iron Oxide	FeO_x	1.8-2.0	Paramagnetic, easy for magnetic separation	39, 66
Manganese Oxide	MnO	3.0	Poor electron conductivity	44, 66
Silicon Oxide	SiO_2	9.1	Good insulator; porous, allows access to catalytic core	66-67

structure of the system. This modification can either benefit or hinder the desired catalysis process, analogously understood through the investigation of graphene in nanoelectronics.[68] Therefore, it can clearly be seen that a complete description of the core-shell structure requires a full quantum mechanical analysis, including all possible variations to the structure, to fully explain experimental results. This topic, however, is outside the scope of this document, and only mention of the core-shell structures used and the results obtained are presented.

Core-Shell Syntheses

Seed-mediated Growth

Seed-mediated growth is the process during which noble metal nanoparticles are synthesized first, producing the seed, followed by formation of the oxide shell around the noble metal core. This is the most common process in developing the core-shell structures. This method of synthesizing core-shell heterostructures requires epitaxial growth of the metal oxide shell onto the noble metal core. It is believed that this type of growth requires a certain amount of lattice mismatch (<2%) between the core and shell.[69] The interfacial energy between the noble metal core and the metal oxide shell can be attributed to this lattice mismatch.[70-73] Several reports point out that a porous oxide shell is necessary because the catalysis is believed to occur at the noble metal core, between the shell and core matrices and not at the shell exterior.[74-75]

The gold-copper(I) oxide core-shell structure (Au@Cu_2O) has been widely investigated over the last few years.[65, 76-79] Liu et al. found that gold and copper had a 4.5% lattice mismatch, which is why the cuprous oxide shell forms a compact shell as opposed to amorphous islands over the gold core. They synthesized gold nanoparticle seeds by mixing chloroauric acid ($HAuCl_4 \cdot 3H_2O$) and water under reflux followed by an injection of trisodium citrate solution and further refluxed to obtain Au seeds with a diameter of approximately 60 nm. Under an ice bath, polyvinylpyrrolidone (PVP), sodium citrate (as a reducing agent), and copper

sulfate ($CuSO_4$) were added to the Au seed solution. The mixture was then diluted with sodium hydroxide (NaOH) and ascorbic acid to create Au@Cu_2O core-shell structures with the core size retaining its diameter of 60 nm and a copper(I) oxide (Cu_2O) shell approximately 20 nm thick. This structure is shown in the scanning electron microscopy (SEM) and transmission electron microscopy (TEM) images (Figure 5).[76] Similarly, Kong et al. synthesized gold nanorod (NR) seeds by mixing $HAuCl_4 \cdot 3H_2O$, cetyltrimethylammonium bromide (CTAB), and a solution of ice-cold sodium borohydride ($NaBH_4$) in water. Another solution of CTAB, water, $HAuCl_4 \cdot 3H_2O$, silver nitrate ($AgNO_3$), and ascorbic acid was called the "growth" solution to which the seed solution was injected while stirring at 26 °C for 12 hours to produce the Au NRs. In order to get a Cu_2O shell with octahedral framework they added the Au NR solution to a solution containing copper(II) nitrate trihydrate ($Cu(NO_3)_2 \cdot 3H_2O$), sodium dodecyl sulfate (SDS), and water, followed by the addition of NaOH and then adding dropwise a hydrazine hydrate and water solution. Size of the products could be predicted and controlled by adjusting the volume of Au seed solution. Average edge size of the octahedral was 158 nm, as can be seen in the high-annular angle dark field (HAADF) STEM image in Figure 6.[65]

The morphology of the shell can be controlled. Wang et al. synthesized rhombic dodecahedral and edge- and corner-truncated gold nanoparticles to control the overall morphology of the Au@Cu_2O core-shell heterostructures (Figure 7). Rhombic dodecahedra gold nanocrystals had a diameter of ~90 nm, and with varying amounts of the reductant (hydroxylamine hydrochloride, $NH_2OH \cdot HCl$) they were able to obtain cubic, cuboctahedra, and octahedral structures with average diameters of 304, 345, and 373 nm, respectively. Edge- and corner-truncated octahedral gold nanocrystals had a diameter of ~85 nm, and while increasing the volume of the reductant, they were able to obtain heterostructures that evolved from face-raised cubic to cuboctahedral and

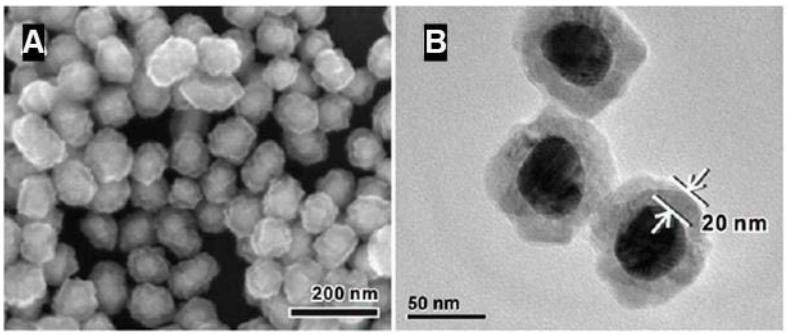

Figure 5. A) SEM image and B) TEM image of Au@Cu_2O core-shell NPs with the shell thickness about 20 nm. Figure modified from reference.[76]

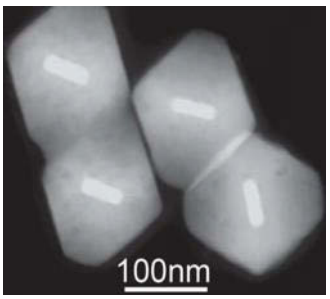

Figure 6. HAADF-STEM image of AuNR@Cu_2O heterostructure. Figure modified from reference.[65]

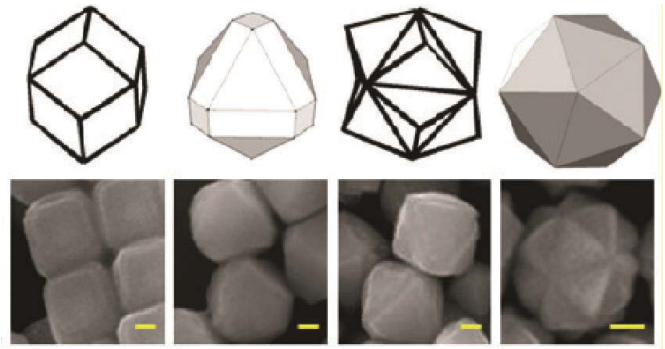

Figure 7. Different Au core nanoparticle structures (top) forming different Cu_2O shell configurations (bottom) with a scale bar = 100 nm. Figure modified from reference.[78]

truncated octahedral structures with average diameters of 283, 331, and 363, respectively. Icosahedral gold nanocrystals could produce Au@Cu_2O core-shell stellated icosahedra and truncated stellated icosahedra structures by increasing the reductant volume. The trisoctahedral gold nanocrystals had diameters of ~90 nm, and with varying amounts of the reductant they could get cubic, cuboctahedra, and face-raised octahedral structures, in order of increasing reductant, with diameters of 340-380 nm. Au@Cu_2O core-shell cubes and face-raised cubes were shown to be inactive in the photodegradation of methyl orange, but face-raised octahedral was shown to have the best catalytic performance, with octahedral structures to be the second runner up. They believe that the presence of v-shaped edges with the gold core enhances the catalytic activity.[78]

One of the advantages of having an iron oxide shell as opposed to a different metal oxide is that the catalyst has the potential to be easily recovered using magnetic separation, which is one of the major reasons why it is so attractive for this type of structured catalyst.[39] Lin and co-workers created gold-iron(II,III) oxide (Au-Fe_3O_4) flower-like and dumbbell shaped structures using thermal decomposition of an iron oleate complex ($Fe(OL)_3$) in the presence of Au seeds that ranged between 5-10 nm and refluxed at 310 °C. When the Au seeds were small dumbbell shaped heterostructures with a diameter of 12-16 nm were formed and when larger Au seeds were used (7-13 nm) flower-like heterostructures in the range of 20-28 nm were produced (Figure 8). Similarly, Yin et al. have synthesized gold-iron(III) oxide (Au@Fe_2O_3) core-shell structures, but used thiolated gold nanoparticle seeds instead of PVP or other applicable ligand, to control the iron oxide shell.[40] $HAuCl_4 \cdot 3H_2O$, water, tetraoctylammonium bromide (TOABr), and toluene were vigorously mixed; to which 1-dodecanethiol and $NaBH_4$ were added with continued stirring followed by separation of the organic phase to obtain thiol coated gold nanoparticles. The thiolated gold nanoparticles were then coated with iron pentacarbonyl ($Fe(CO)_5$), attached to a support and then pretreated to remove the thiol ligands to obtain Au@Fe_2O_3 core-hollow shell nanoparticles. The average size of the Au nanoparticles were estimated to be 2.5 nm with varying Fe_2O_3 shell

thicknesses of 1, 2, 3, and 4 nm, depending on the amount of $Fe(CO)_5$ added. This core-shell structure was then loaded onto a silica (SiO_2), titania (TiO_2), carbon (C), or α-Fe_2O_3 support.[40]

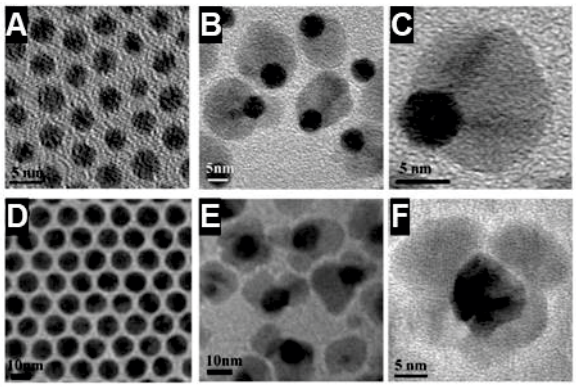

Figure 8. TEM images of A) 5 nm Au NPs, B) dumbbell-like Au-Fe_3O_4 heterostructures, D) 10 nm Au NPs, and E) flower-like Au-Fe_3O_4 heterostructures; C) and F) are high-resolution transmission electron microscopy (HRTEM) images of dumbbell- and flower-like Au-Fe_3O_4 heterostructures, respectively. Figure modified from reference.[39]

Cobalt(II,III) oxide (Co_3O_4) is considered to be very active to catalyze the oxygen evolution reaction (OER) when combined with a conductive metal core. Yan's group produced such a structure employing a gold core encapsulated by a cobalt oxide shell. They reduced $HAuCl_4 \cdot 3H_2O$ with tert-butylamine borane (TBAB) and utilized oleylamine as a surfactant to create Au NCs. This was followed by epitaxial growth of cobalt oxide onto the Au NCs with cobalt(II) acetylacetonate ($Co(acac)_2$) and TBAB in conjunction with oleylamine and oleic acid, then loaded onto carbon and calcined in air. As a result, gold-cobalt oxide core-shell structures (Au@Co_3O_4) with a core diameter of ~3.5 nm, a shell thickness of 2 nm, and an overall diameter of about 8 nm were successfully synthesized. However, the cobalt oxide shell appeared to be amorphous.[41]

Another synthesized core-shell nanoparticle of interest is gold-zinc oxide (Au@ZnO) core-shell structures.[70] It was synthesized by first stabilizing the gold NPs with citrate and then treating them with a thiol ligand, 4-mercaptobenzoic acid, at 60 °C for 2 hours. After isolation, the gold nanoparticles were dispersed in a PVP solution with hexamethylenetetramine (HMTA) and zinc nitrate ($Zn(NO_3)$), and subsequent incubation yielded the desired core-shell structure. The use of PVP was found to be a critical step in tuning the interfacial energies, controlling the epitaxial growth, and stabilizing the overall structure. The efficacy of PVP rests in its complex charge distribution, where the non-polar end interacts with the hydrophobic thiol ligands attached to the gold core and the polar end interacts with the ZnO shell (Figure 9). The resulting gold cores were measured to be 40 nm in size with a shell of 40 nm thick, making the heterostructure 120 nm in diameter.

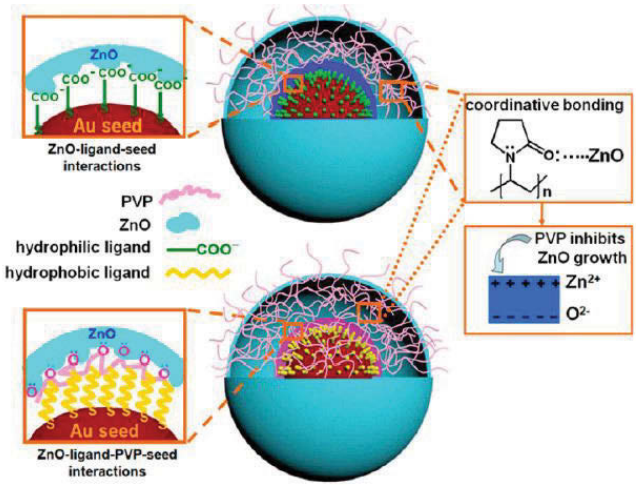

Figure 9. The Au−ligand−ZnO and the Au−ligand−PVP−ZnO interactions in Au@ZnO heterostructures. Figure modified from reference.[70]

Aside from the dense-packed Au-oxide NPs, yolk-shell heterostructures have also been created. Lin et al. synthesized three different yolk-shell heterostructures, all using a mesoporous silicon oxide shell ($mSiO_2$) and a gold core NR. The Au NR was surrounded by silver (Ag), which was then surrounded

by $mSiO_2$ (AuNR@Ag@$mSiO_2$). Another with a Au core NR surrounded by another Au layer and then by $mSiO_2$ (AuNR@Au@$mSiO_2$), and finally a yolk-shell structure with a gold NR core within a void gold shell which was then surrounded by $mSiO_2$ (AuNR@void@Au@$mSiO_2$). The gold NR seeds were first synthesized by combining $HAuCl_4 \cdot 3H_2O$, CTAB, and a cold solution of $NaBH_4$ and water. Then, after 2 hours this solution was added to another solution containing $HAuCl_4 \cdot 3H_2O$, CTAB, $AgNO_3$, and L-ascorbic acid. For all three nanostructures, the Au NR seeds were dispersed in water with NaOH, and 20% tetraethyl orthosilicate (TEOS), which generated AuNR@$mSiO_2$ structures. In order to prepare the core-shell AuNR@Ag@$mSiO_2$ structure, the AuNR@$mSiO_2$ solution was combined with water, hydroquinone, sodium citrate, citric acid (to adjust to pH of 4), and $AgNO_3$ at 60 °C (Figure 10). In preparing the AuNR@Au@$mSiO_2$ structure, the AuNR@$mSiO_2$ solution was mixed with water, a $HAuCl_4$ solution, and ascorbic acid. To prepare the yolk-shell AuNR@void@Au@$mSiO_2$ structure, a solution of the AuNR@Ag@$mSiO_2$ particles was injected with varying volumes of $HAuCl_4$ solution. In order to control the shell thicknesses, the authors simply varied the volume of TEOS that was added to the initial AuNR@$mSiO_2$ structures.[80]

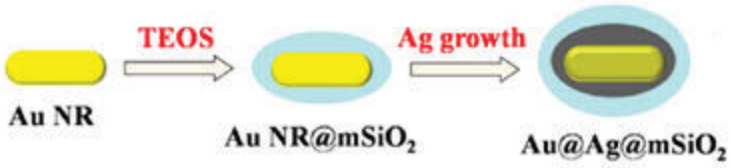

Figure 10. Fabrication of the AuNR@Ag@$mSiO_2$ core-shell structures. Figure modified from reference.[80]

The core-shell heterostructure containing a tin oxide shell (Au@SnO_2) was synthesized by Tripathy et al. where the gold core was synthesized using the common reduction of $HAuCl_4$, which was combined with trisodium citrate dehydrate and water while heated. An ultrasound assisted method was used for

the seeded growth of the Au@SnO_2 heterostructure by adding NaOH (to adjust pH to 10) and sodium hexahydroxostannate ($Na_2SnO_3 \cdot 3H_2O$) for which the shell formation was monitored via UV-visible spectroscopy. After the tin containing reagent was added, the solution reacted for 90 minutes and then was washed with water, to obtain the Au@SnO_2 core-shell structure with a gold core of 10-12 nm with face-centered cubic conformation and a SnO_2 shell that was 10 nm thick with tetragonal geometry.[42] The same method was adapted by Chung et al. to produce gold cores of 10 nm with a SnO_2 shell of 8 nm.[81] Similarly, Wu and co-workers prepared silver core and tin oxide shell (Ag@SnO_2) nanoparticles. Briefly, they combined $AgNO_3$, water, $NaBH_4$, and trisodium citrate. Then, NaOH (to adjust pH to 10) and $Na_2SnO_3 \cdot 3H_2O$ were added at four intervals, every 30 minutes, while heated to 60 °C to obtain the desired core-shell structure. The silver core had a diameter of approximately 15 nm and the SnO_2 shell was roughly 10 nm thick.[82]

Titanium oxide has been a common and popular choice as an oxide shell because of its thermal stability[57] and electronic properties.[49] Chen et al. synthesized Au@TiO_2 core-shell structures by combining a $HAuCl_4$ solution, sodium citrate solution, and PVP with heat, and afterwards added a titanium(IV) butoxide solution with ethanol to obtain the gold seeds. TiO_2 was then nucleated onto the gold core surface, purified by semipermeable membrane technique, dried, and then varying samples were annealed to 300 °C, 500 °C, and 700 °C. The gold core had a diameter of 10-15 nm and the shell was 1-3 nm thick. Although the shell was not uniform, they assured that there was complete coverage of the gold core. Without any post-heating, the TiO_2 shells were amorphous, while heating to 300 °C and 500 °C produced anatase TiO_2 shells and heating to 700 °C produced rutile TiO_2 shells. In each case, however, it is important to note that the gold core showed no oxidation and was in a metallic state (Au^0).[74] Yin's group followed the same procedure, but used titanium tetraisopropoxide (TTIP) instead of titanium(IV) butoxide,[83] while Fang et al. used $TiCl_3$ and poly(sodium 4-styrenesulfonate) (PSS).[84] Gold is the only noble metal that does not have a stable oxidation state.[85] This synthesis can be extended to silicon oxide shells using the PVP ligand[86] and

without the PVP ligand, using a silane coupling agent instead,[87-88] cerium oxide shells that use a reductant other than sodium citrate,[89-90] and even bimetallic colloids (Au@Ag).[91] Xu's group produced the same flower-like core-shell structures, but, in addition to Au, also synthesized the titania shell with platinum (Pt) and palladium (Pd) cores. The only reported core-shell structure dimensions reported for these heterostructures was a wide range of 250-450 nm.[56] Wu et al. also synthesized a Pt@TiO_2 core-shell structure similar to Zhang's procedure with only a few modifications, which allowed them to get different structures; instead of flower-like structures the shell formed wedge shaped petals.[49] Bakhmutsky's and co-workers did a combination of palladium or platinum cores with titania or zirconia shells. They were able to produce noble metal cores of 2 nm in diameter and amorphous metal oxide shells that were 2-4 nm thick for the titania shell and 2-3 nm thick for the zirconia shell.[63]

Moreover, the yolk-shell structure has been achieved in Au-metal oxide nanostructures. For example, Au@ZrO_2 yolk-shell heterostructures that were prepared by Schüth's group. The Au core was first coated with silica, which served as a sacrificing template and was leached away after coating with zirconia. For the zirconia shell, the prior resulting solution was then injected with Lutensol AO_5 followed by zirconium(IV) butoxide ($Zr(OBu)_4$) and after 1 hour of stirring left to sit for 3 days. The colloid was then treated with NaOH for 16 hours followed by a fresh solution of NaOH for 12 h more in order to remove the silica layer. The resulting solution was washed with water and ethyl t-butyl ether to obtain the Au@ZrO_2 yolk-shell structure (Figure 11).[62, 92]

A Au core with a cerium oxide shell (Au@CeO_2) was synthesized by Qu et al. by first preparing Au@GCEC (GCEC, the gel of citric acid-ethylene glycol-Ce^{3+}), which was the precursor to Au@CeO_2, by combining Au NPs, citric acid, ethylene glycol and Ce^{3+} ions under a 500 W Xe (xenon) arc lamp which irradiated the mixture. The Au@GCEC precursor created a shell 1-13 nm thick depending on the length of irradiation time applied. Once the Au@GCEC structure was calcined it

produced Au@CeO_2/SiO_2 giving a gold core of about 17 nm and a CeO_2 shell of 8 nm thick.[93] Li and co-workers also synthesized a Au@CeO_2 structure using CTAB as a stabilizer, while sequentially adding an EDTA-NH_3 mixture and a cerium nitrate ($Ce(NO_3)_3$) solution.[94]

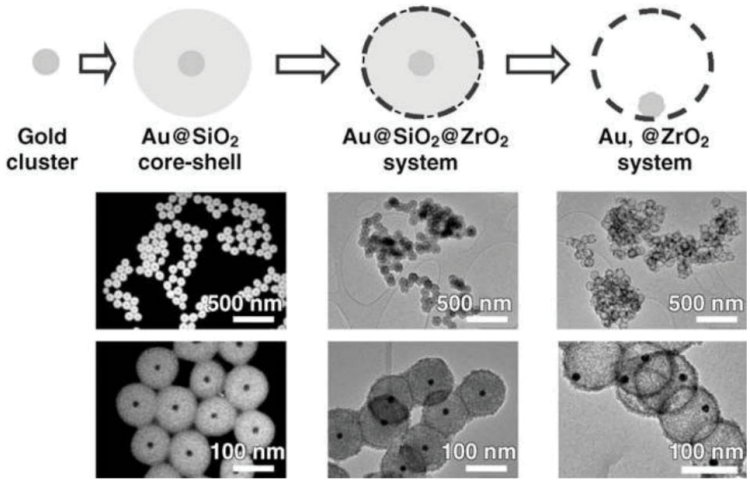

Figure 11. Fabrication process of Au@ZrO_2 yolk-shell structure and TEM images at each stage. Figure modified from reference.[92]

Post Selective Oxidation Treatment

Another popular methodology to fabricate core-shell structures is through post selective oxidation. This process is typically applied in bimetallic systems, of which upon heating/annealing/calcining the easily oxidized component can be drawn out, leaving the noble metal as the core with a metal oxide shell. This method provides great flexibility for the composition of metal core and oxide shell by choosing various bimetallic starting materials. However, with this process it seems to be very difficult to fine-tune the shell thickness surrounding the core of which can typically be accomplished using seeded growth.

The Au@MnO core-shell structure was synthesized by mixing gold nanoparticles, manganese(II) acetylacetonate ($Mn(acac)_2$), and potassium

triethylborohydride ($KBEt_3H$) at high temperatures to create a AuMn alloy. The strong reducing agent, $KBEt_3H$, was used here to reduce Mn^{2+} to Mn^0. The AuMn alloy was then annealed in air at 170 °C to create the Au@MnO core-shell heterostructures that were about 5 nm in diameter [44]. The core-shell structure formation was highly dependent on the Au:Mn ratio and only when the ratio was closest to one, $Au_{44}Mn_{56}$ (Figure 12A), was the core-shell Au@MnO formed. Otherwise, when the Au:Mn ratio was greater than one, flower-like structures were formed ($Au_{67}Mn_{33}$) and, when the Au:Mn ratio was a lot lower than one, dumbbell shaped structures were formed ($Au_{35}Mn_{65}$) as seen in Figure 12B.[44]

Using a self-templating technique, Qi et al. synthesized the Au@CeO_2 core-shell structure, where $HAuCl_4 \cdot 3H_2O$ and $CeCl_3$ are mixed in an aqueous solution containing glucose and urea under hydrothermal conditions, followed by the post selective oxidation treatment by calcination (Figure 13A). They produced nanoparticles of about 178 nm in diameter with a gold core of roughly 17 nm while the CeO_2 shell was composed of nanoparticles of about 9 nm (Figure 13B).[75]

Zhu et al. synthesized the Au@TiO_2 core-shell structure via a reverse micelle method followed by annealing. The Au@TiO_2 core-shell heterostructures had a diameter of about 20 nm, with a gold core size of 9-12 nm and a titania shell 3-5 nm thick. The core-shell structures showed some non-uniformity in the shell thickness, but the gold cores were fully enclosed.[45] Kaneda's group also utilized the reverse micelle method to create a Au@CeO_2 core-shell structure. A micelle solution containing Au^{3+} and Ce^{3+} was combined with NaOH to yield the core-shell structure containing the Au^0 and Ce^{4+} oxidation states. They obtained Au cores with a diameter of 8.6 nm surrounded by spherical CeO_2 NPs that were 2 nm in diameter with a shell thickness of ~5.5 nm for heterostructures of 20 nm thick.[46]

Au@SnO_2 core-shell structures were formed by Xie's group with gold cores of 15 and 40 nm with a shell thickness of 6-7 nm for both seed sizes. A $SnCl_2$ solution, pre-made Au nanoparticle seeds and $NaBH_4$ were mixed. Then, the AuSn alloy, dispersed in ethanol, was distributed onto a silicon support and air dried

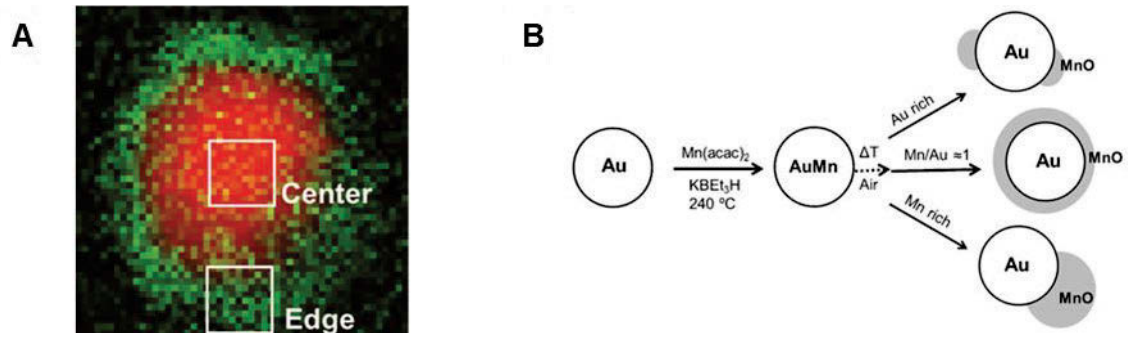

Figure 12. A) STEM-EELS 2D mapping of C-$Au_{44}Mn_{56}$ after annealing and B) synthesis of Au-MnO heterostructures. Figure modified from reference.[44]

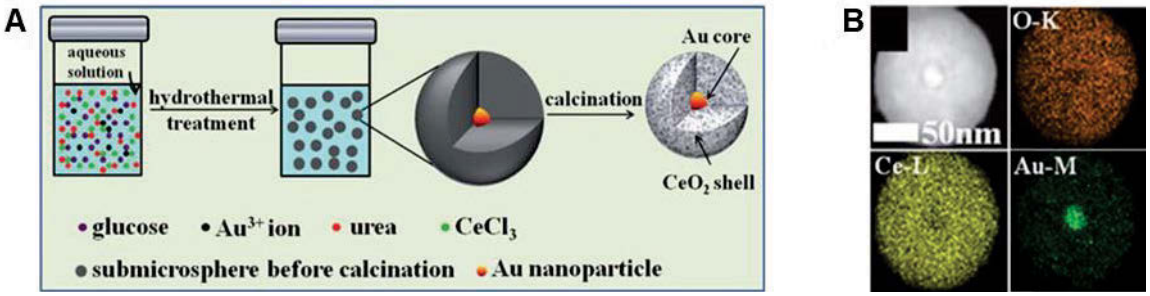

Figure 13. A) Synthesis of Au@CeO_2 core-shell structures and B) HAADF-STEM mapping image of one Au@CeO_2 heterostructure. Figure modified from reference.[75]

before being annealed at 850 °C to create the noble metal core-metal oxide shell structure. There were small defects in the SnO_2 shell due to the different diffusion rates of the oxygen and tin atoms, for which the oxygen atoms were faster. These defects may offer more pathways for interacting molecules to directly contact the catalytic core.61

One-Pot Chemical Synthesis

One-pot synthesis refers to the simultaneous formation of both the noble metal cores and the metal oxide shells. This is not a widely applied synthesis for core-shell structures because it is hindered by the difficulties of fine tuning core-shell structures and controlling their morphology. However, it is a popular tactic to attempt for its ease and simplicity, especially where industrial purposes are concerned.

Dong's group used reverse micelle systems that contained an aqueous solution of $HAuCl_4$ and another containing $TiCl_3$ and then simply combined all reagents and stirred the solution for 1 hour at 60 °C to obtain Au@TiO_2 core-shell structures (Figure 14A). The aqueous solution formed reverse micelles in cyclohexane and poly(oxyethylene) nonylphenyl ether, which acted as the constrained reaction system for the redox reaction between Au^{3+} and Ti^{3+} to form nanosized particles. They obtained a gold core of size 40 nm and a TiO_2 shell of 5nm thick (Figure 14B-C).[95]

Using a new gas bubbling-assisted membrane reduction-precipitation (GBMR/P) method, created by Wei et al. specifically for this synthesis, this group was essentially able to turn a multi-step process into a one step process. Into Beaker I (Figure 15A), they added a PVP solution, $HAuCl_4 \cdot 3H_2O$, the zirconia support (ZrO_2), and cerium nitrate ($Ce(NO_3)_3 \cdot H_2O$). Then, to Beaker II, they added $NaBH_4$ and, once it was consumed, a precipitating agent ($NH_3 \cdot H_2O$). Hydrogen gas was used for bubbling which aided in creating a homogeneous mixture and continued to bubble the mixture for 1 hour after everything was added and then calcined to 500 °C to obtain the Au@CeO_2 core-shell structure (Figure 15B). The

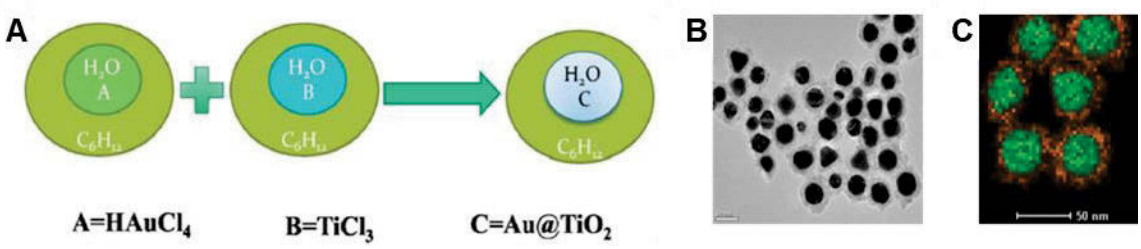

Figure 14. A) Synthesis of Au@TiO_2 core-shell heterostructure using reverse micelle method B) TEM and C) elemental mapping of Au@TiO_2 core-shell heterostructure. Figure modified from reference.[95]

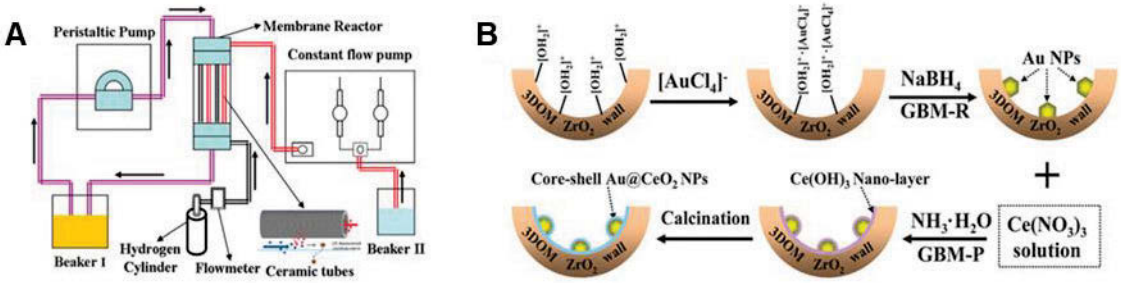

Figure 15. A) Diagram of the gas bubbling-assisted membrane reduction-precipitation (GBMR/P) device for synthesis of ZrO_2-supported Au@CeO_2 core-shell heterostructure B) one-pot synthesis of Au@CeO_2/ZrO_2 using the GBMR/P method. Figure modified from reference.[47]

thickness of the CeO_2 shell was 1-2 nm, while the size the Au@CeO_2 heterostructure over the ZrO_2 support were 3-11 nm in diameter (mean diameter 3.7 nm).[47]

A core-shell structure of Ag@MSNs (MSNs = mesoporous silica spherical nanoparticles) was synthesized by combining $AgNO_3$, formaldehyde, CTAB, TEOS, and NaOH at 80 °C, and then removing the CTAB with an ethanol solution. Synthesized by Han et al., these heterostructures were approximately 65 nm in diameter with a silver core of about 15 nm.[96]

Similarly, using a one-pot hydrothermal process, a Ag@Fe_3O_4 flower-like core-shell heterostructures were synthesized by Jiang's group by combining polyacrylamide (PAM), sodium citrate, $Fe(NO_3)_3$, and $AgNO_3$, all in an aqueous solution. Nanostructures were roughly 200 nm with Ag core sizes ranging from 50 to 100 nm and had a non-ordered mesoporosity, where the pore sizes were found to be around 7.5 nm. By varying the concentrations of the silver and iron containing precursors they found that the core size could be adjusted; increasing the Ag concentration increased the core size while increasing the Fe concentration decreased the core size.[97] Both Jiang's and Han's methods are considered to be green chemistry because there were no harmful reagents utilized. The Ag@ZnO core-shell structure was synthesized by Aguirre et al., which had Ag nanoparticles of sizes 20-30 nm, surrounded by 10 nm of ZnO units.[54]

Au-Metal Oxide Core-Shell Structures: CO Oxidation

Shell Thickness on Catalytic Activity

For CO oxidation, it was shown that the Au@Fe_2O_3/SiO_2, Au@Fe_2O_3/TiO_2, Au@Fe_2O_3/C, and Au@Fe_2O_3/Fe_2O_3 core-shell catalysts were more active than their non-encapsulated versions, Au/SiO_2, Au/TiO_2, Au/C, and Au/Fe_2O_3, respectively. However, using different supports for the Au@Fe_2O_3 core-shell structure (with a shell of 2 nm) did not seem to affect its catalytic activity. In studying the shell thickness and its effect on catalytic activity, where the Au core

was approximately 2.5 nm and the iron oxide shells were 1, 2, 3, and 4 nm thick, it was found that the CO conversion for these structures at -40 °C were 85%, 32%, 44%, and 23%, respectively. The thinner the metal oxide shell, the greater the CO conversion and also the larger the rate of the reaction for the conversion.[40]

Core Size on Catalytic Activity

Not only does shell thickness affect catalytic activity, but the size of the noble metal core can also play an important role in the effectiveness of the catalyst. In order to study the effect of the core size on CO oxidation, Zhang's group synthesized gold cores of varying sizes with a ceria shell. They found that the CO conversion of Au@CeO_2/SiO_2 was indirectly proportional with the gold core particle size, increasing with decreasing gold particle size, where they tested gold core sizes of 11, 17 and 32 nm.[93] Using a TiO_2 shell with a Au core, Chen et al. also discovered that CO oxidation was dependent on the size of the gold core within the core-shell nanoparticle. It was determined in previous studies that CO conversion was more successful with a small catalyst (between 2-5 nm),[11] however, in this particular study, they synthesized a gold core size of 10-15 nm and were still able to attain half CO conversion at 220 °C.[74] Han et al. likewise synthesized a Au@TiO_2 core-shell structure with a gold core of 40 nm and TiO_2 shell of 5 nm thick. The non-encapsulated gold NPs (Au/TiO_2) showed better CO oxidation activity on the first cycle, but quickly deteriorated, whereas the core-shell structure did not show any alteration after several cycles.[95]

It was found that Au@SiO_2 core-shell structures were also functional for CO oxidation and it was further discovered that they were dependent on the size of the gold core. Zhang et al. synthesized gold nanoparticle cores of sizes 1.5, 1.8, and 2.3 nm with corresponding SiO_2 shells of 8.6, 10, and 11 nm thick, respectively. The smaller the gold core, the higher catalytic activity at lower temperatures (Figure 16). At 100 °C, the turnover frequency (TOF) for the gold core sizes of 1.5, 1.8, and 2.3 nm were 96.2, 46.3, and 6.64 h^{-1}, and they each had 100% CO conversion at temperatures of 180 °C, 260 °C, and 400 °C, respectively. They

concluded that the smaller the gold core size, the better the catalytic activity for CO oxidation, however, they did not have consistent shell thicknesses for their particles, which in itself could have hindered or enhanced the catalytic activity.[67] Guttel et al. synthesized a Au@ZrO_2 yolk-shell structure while also studying the size effects of the noble metal core with the catalytic activity of CO oxidation. They were able to adjust the size of the gold core via leaching from which they obtained varying gold core sizes between 5 and 15 nm. Unlike other studies, they were not able to find a strong correlation between decreasing noble metal core size and CO conversion. They proposed that it was because they would not expect to see a strong correlation unless the gold cores were less than 5 nm[98] However, the lack of correlation could simply be due to the yolk-shell structure instead of a more symmetric core-shell structure. A yolk-shell structure would have more hollow/void spaces between the core and shell, and thus it would not have the complete synergistic effects of the core-shell interface that a core-shell structure would be expected to have.

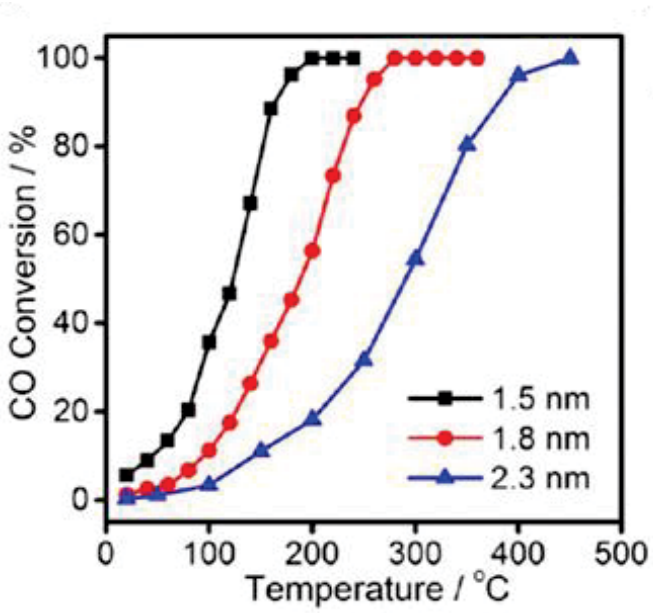

Figure 16. CO conversion vs. temperature by Au@SiO_2 heterostructures of varying gold core sizes. Figure modified from reference.[67]

Core-Shell Interfacial Synergies

A study by Galeano et al. indicated that the Au@ZrO_2 core-shell structures demonstrated at least one order of magnitude higher CO oxidation activity when compared with the Au@C structure, (Figure 17).[62] They also compared this structure with Au@ZrO_2/C, where the porous sites on the zirconia shell have been essentially filled by carbon. Given a decrease in the shell's porosity one would expect a decrease in CO conversion as consequence, but they found that the catalytic activity was not reduced or enhanced and that the additional carbon merely added weight to the heterostructure. This leads one to question where CO conversion actually occurs, at the core or in a synergistic relationship between the core and shell, at the shell's surface.

Core-Shell vs. Non-encapsulated Catalyst Counterparts

A diesel oxidation catalyst (DOC) reduces emissions from diesel fueled vehicles and equipment by oxidizing CO and unburned hydrocarbons, as well as enabling a good NO/NO_2 ratio for the selective catalytic reduction of NO_x with NH_3. When compared to the standard Pt/Al_2O_3 catalyst at temperatures below 150 °C, Bauer et al. found that the Au@CuO/SiO_2 catalyst was much more active, but was inhibited by propylene and nitrogen monoxide (NO).[99] Yu et al. synthesized a Au@SnO_2 core-shell structure, using seeded growth. With a gold core of 15 nm size and a shell of 6-7 nm thick, the Au@SnO_2 core-shell structures had a half CO conversion around 230 °C, while the non-encapsulated Au/SnO_2 had a half CO conversion around 330 °C as well as suffering a substantial loss in activity compared to the core-shell structure (Figure 18). The core-shell structure had a high-temperature stability (heated to 850 °C) and was thought to also be utilizing the synergetic confinement effect, as well as the strong interactions between gold and the oxide support, for which both may enhance its catalytic performance for CO oxidation.[61]

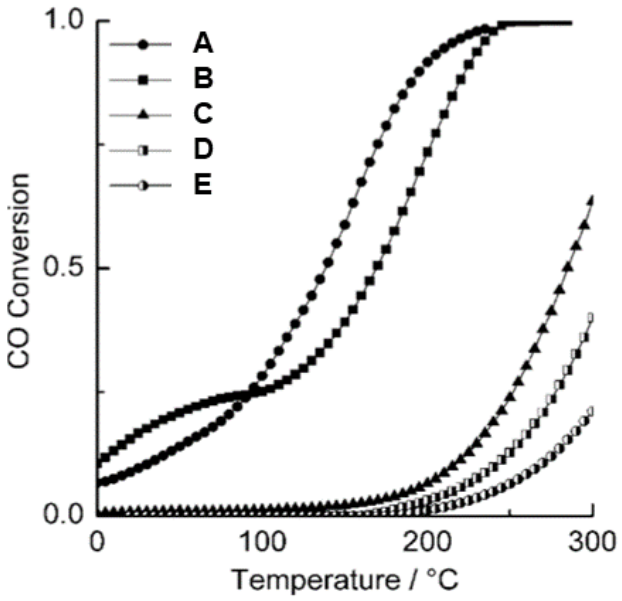

Figure 17. Conversion temperature curves for CO oxidation (a-d: Au core of 14 nm). A) Au@ZrO_2, B) Au@ZrO_2,C, C) Au@C silica route, D) Au@C zirconia route, E) Au@C zirconia route (Au core of 7 nm). Figure modified from reference.[62]

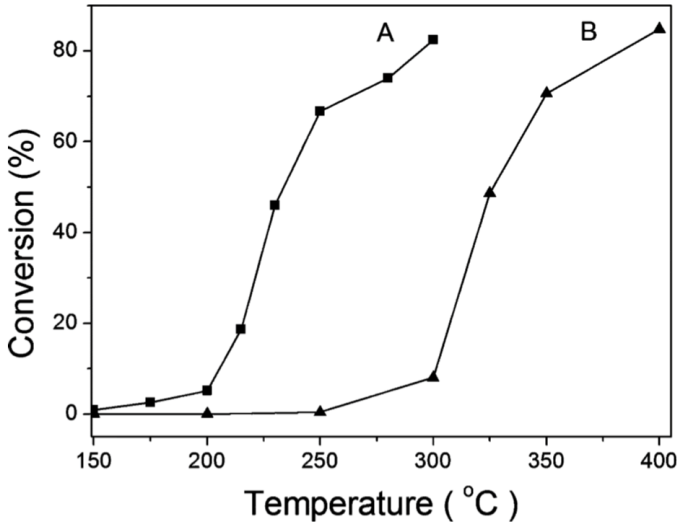

Figure 18. CO conversion using A) Au@SnO_2 core-shell structure and B) non-encapsulated Au/SnO_2 catalysts. Figure modified from reference.[61]

CHAPTER THREE

MATERIALS AND METHODS

Part of the information in this chapter is taken from Michelle Lukosi et al. paper, currently under editing.

Materials

The chemical reagents used were hydrogen tetrachloroaurate trihydrate ($HAuCl_4 \cdot 3H_2O$), 1-hexanethiol (SHC_6H_{13}, 98%), tetraoctylammonium bromide (TOABr, 98%), sodium borohydride ($NaBH_4$, 99%), iron pentacarbonyl ($Fe(CO)_5$), oleylamine (reagent grade), oleic acid (90%), and Cab-O-Sil (fumed silica). Solvents used were methanol, deionized water, toluene, acetone, ethanol, dichloromethane, hexanes, and diphenyl ether. All chemicals listed were used as obtained and without any further purification.

Catalyst Preparations

In preparing the Au_{144} clusters, Qian's methods were utilized.[27] In ambient conditions, 0.70 millimole (mmol) of $HAuCl_4 \cdot 3H_2O$ was added with 0.70 mmol TOABr in methanol in a round bottom flask. The solution changes color from yellow to red once the TOABr is added, indicating the formation of Oct_4N^+ $AuBr_4^-$. After ~20 minutes, 1.505 mmol of 1-hexanethiol are added to the solution at room temperature and the color of the reaction mixture turns a creamy white color over the course of 30-60 minutes. The thiol;Au ratio was adjusted to 4.3:1.[35] After 1 hour, a fresh solution of $NaBH_4$ (3.5 mmol) in cold DI water is rapidly added to the solution under vigorous stirring. The color of solution immediately turns black with a slightly exothermic reaction and produces Au clusters, that precipitate out of the methanol solution. The reaction continues to stir for 5 hours to completely equilibrate the reaction. The black precipitates are collected by centrifugation (6 minutes at 6500 rpm) and decantation. The black precipitates are washed with excess methanol and collected by centrifugation several times to completely

remove all small-molecule and electrolyte residue, including excess free thiol residues. Then, toluene is used to separate the Au clusters from Au(I)-SR polymers, which are poorly soluble in most solvents. The as-obtained solution only contains $Au_{144}(SR)_{60}$ (major product) and $Au_{25}(SR)_{18}$ (minor product). Acetone is used to separate the $Au_{144}(SR)_{60}$ and $Au_{25}(SR)_{18}$ clusters. The $Au_{144}(SR)_{60}$ is dispersed into hexane, toluene, or dichloromethane depending on the characterization method to be used.

In coating the cluster with an iron oxide shell, methods from Yin *et al.* were applied,[40] following a seed-mediated post selective oxidation treatment technique (Figure 19). In a 4-neck 100 milliliter (mL) round-bottom flask, 50 mL of diphenyl ether, 0.15 mL of an oleylamine, and 0.15 mL oleic acid were added, stirred, and heated to 65 °C. Then, 20 mg of Au_{144} cluster dispersed in 2 mL of toluene is added to the mixture. The solution is set to stir under nitrogen (N_2) flow and heated at 65 °C for 15-20 minutes in order to purge the system of oxygen. The reaction is then put under a nitrogen blanket before adding the iron pentacarbonyl in varying amounts. The flask is slowly heated to 200 °C (~1 °C per minute) and left to stir for 30 minutes. The reaction is then cooled to approximately 105 °C and then the N_2 environment is removed and air is flowed through flask for a minimum of 10 minutes to allow the iron to be drawn out through oxidation. Subsequently, the reaction flask is cooled to room temperature. The solution is washed several times with ethanol and centrifuged. The core-shell precipitate is then dispersed in hexane.

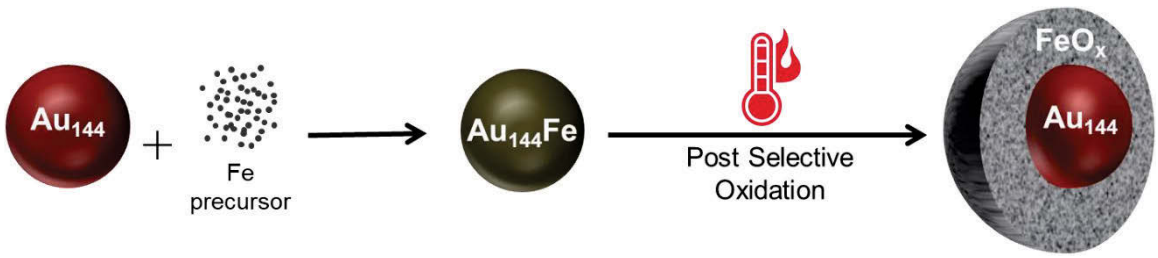

Figure 19. Seed-mediated post-selective oxidation method for $Au_{144}@Fe_2O_3$ particles.

To analyze and test the core-shell structures, they are deposited onto fumed silica (SiO_2) using ~1.5% gold loading. Fumed silica support was utilized because of its inert properties, given its weak metal support interaction (WMSI) and ability to adsorb cations, as opposed to other metal oxide supports that have SMSI's. The silica (Cab-O-Sil) is added to the colloidal mixture of $Au_{144}@Fe_2O_3$ particles in hexane, sonicated, and stirred for 2 hours before slowly evaporating off the solvent, using rotary evaporation. After removing the solvent, the powder is dried and calcined at 300 °C for 2 hours.

Characterizations

X-ray Diffraction

X-ray diffraction (XRD) consists of an X-ray tube, sample holder, and detector. In this research, the X-rays are first generated in a cathode ray tube by bombarding electrons onto a copper (Cu) target. These X-rays are collimated and directed onto the sample where the average composition is determined based on the intensity of the reflected X-rays from the sample. From the peaks in the XRD spectra, the size of the particles can be determined using the Scherrer equation (Equation 1). In this equation, τ represents the mean crystallite/domain size, K equals 0.94 and is a dimensionless shape factor called the Scherrer constant,[100] λ is the wavelength of the X-ray, β is the full width at half maximum (FWHM) of the peak intensity, and θ is the Bragg angle, which are converted to radians.

$$\tau = \frac{K\lambda}{\beta\cos\theta} \quad (1)$$

For this equation we use the 2θ angle. The incident and reflected rays create the angle θ with a crystal plane. Reflections from planes set at θ angle with respect to the incident beam produces a reflected beam at angle 2θ from the incident beam.

The Au_{144} clusters were studied by air drying the clusters dispersed in solution directly onto the silicon plate, which created thin films of the particles. At room temperature, the clusters were analyzed using a PANalytical Empyrean

diffractometer over the range from 10-80° 2θ using Cu K-alpha (K_α) at wavelength 1.540958 Å radiation at 45 kV and 40 mA. The $Au_{144}@Fe_2O_3$ core-shell structures were also characterized by XRD, for which the data of the core-shell structures were collected by studying powder samples and analyzing them using the same instrumentation and parameters as those used for the Au_{144} thin film analyses. The core-shell structures were loaded onto silica via colloidal deposition, calcined, and finely ground to ensure a homogeneous product.

Matrix Assisted Laser Desorption Ionization

One of the methods used to characterize the Au_{144} clusters in this work was a Bruker matrix assisted laser desorption ionization time-of-flight mass spectrometer (MALDI-TOF-MS). MALDI utilizes of the adsorption of laser light by a solid sample layer, for which the laser, in turn, ablates the sample/matrix creating a supersonic plume expansion (Figure 20). This method is typically used with large proteins because it enables very high mass compounds to be analyzed. It is exactly this reason that it is a good characterization method for gold clusters, since Au_{144} NCs are 28.363 killodaltons (kDa) without even including the thiol capping. Matrices used for MALDI are specifically designed to absorb energy via light, which is why they tend to be aromatic compounds. These matrices are typically in solid form and the samples are dispersed in these matrices by co-crystallization either directly onto the sample plate or just before being placed on the sample plate. In order to get a clear spectrum of the compound in question, a specific matrix-to-sample (M-S) ratio is used. A molar M-S ratio that is too low means less laser energy is being transferred into the analyte sample because there are too few matrix molecules. However, a molar M-S ratio that is too high usually means that not enough of the sample is being ablated to produce detectable quantities of ions. Each test has proven to be a case by case basis, where there is a threshold limit, or sweet spot, to each sample's molar M-S ratio.

The mass spectrum was collected in a linear positive ion mode. A dichloromethane solution of the $Au_{144}(SC_6H_{13})_{60}$ particles (5 mg/mL) were mixed

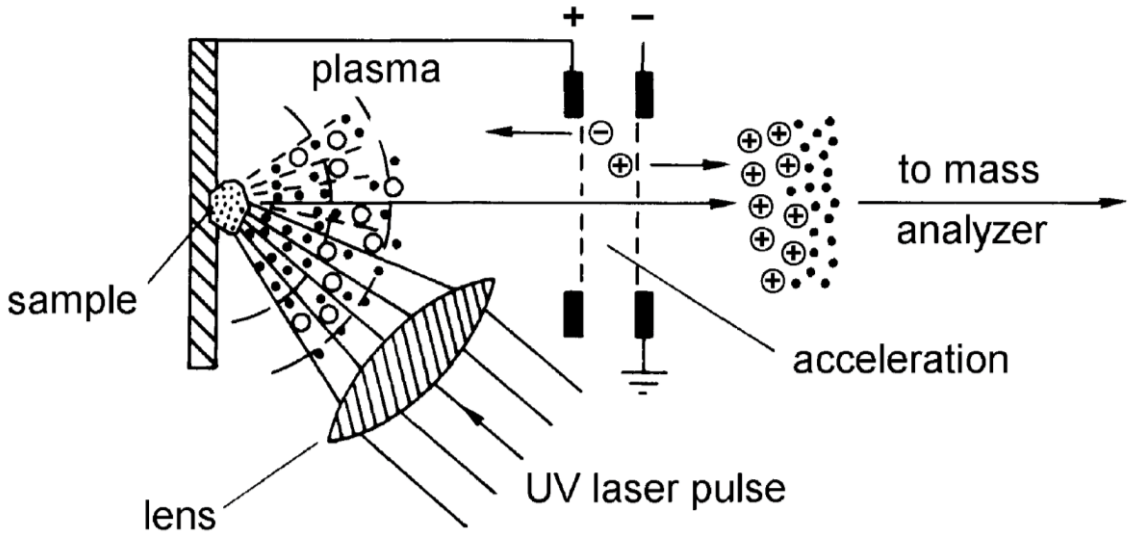

Figure 20. Simplistic laser desorption ion source for non-resonant light absorption by a solid. Figure modified from reference.[101]

with the matrix, a chloroform solution of trans-2-[3-(4-tert-butylphenyl)-2-methyl-2-propenylidene] malononitrile (DCTB) based on literature results,[16, 102-103] (Figure 21) applied to the sample plate (which acts as accelerating electrodes), and then air dried.

Brunauer-Emmett-Teller Analyzer

Adsorption-desorption measurements with N_2 are used to characterize the porosity and surface area of the materials. The Brunauer-Emmett-Teller (BET) method is an extension of the Langmuir theory, which assumes a layer of N_2 gas is adsorbed onto the surface and that the layers do not interact with one another. During adsorption and desorption, the relative pressure of the gas is recorded versus the volume of the tube and mass of sample being analyzed at a constant temperature, which creates the BET isotherm.[104] The nitrogen physisorption isotherms were measured at 77 K using a Micromeritics Gemini 2375 BET area analyzer. The isotherms produced in this research were all type IV isotherms, according to literature.[105] This means that there was a restricted monolayer-multilayer adsorption and a Type IV isotherm can be represented by Equation 2 below, as well as Figure 22, where V is the volume of adsorbed gas, V_m is the monolayer volume, C is the constant, P is the partial pressure of the sample, and P_0 is the saturation vapor pressure of the sample.[105]

$$\frac{P}{V[P_0 - P]} = \frac{1}{V_m C} + \frac{C - 1}{V_m C}\frac{P}{P_0} \quad (2)$$

Inductively Coupled Plasma Optical Emission Spectroscopy

Atomic spectroscopy is good for identifying elements present, as well as, quantifying elemental composition of a compound with trace-metal precision. There are three basic techniques of atomic spectroscopy, absorption, surface fluorescence, and emission. All three techniques involve the process of excitation and decay back down to the ground state.[106] In this research, emission spectroscopy is utilized exclusively. Elemental analysis was done by inductively coupled plasma optical emission spectroscopy (ICP-OES), using an Optima 2100

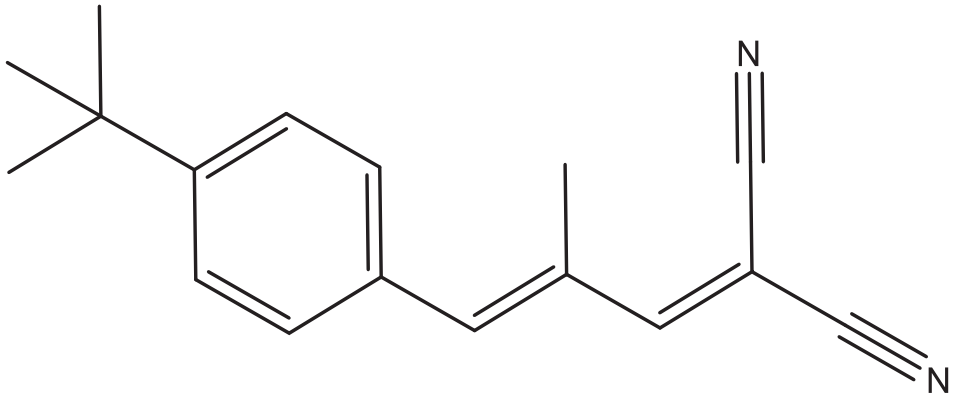

Figure 21. MALDI matrix trans-2-[3-(4-tert-butylphenyl)-2-methyl-2-propenylidene] malononitrile (DCTB).

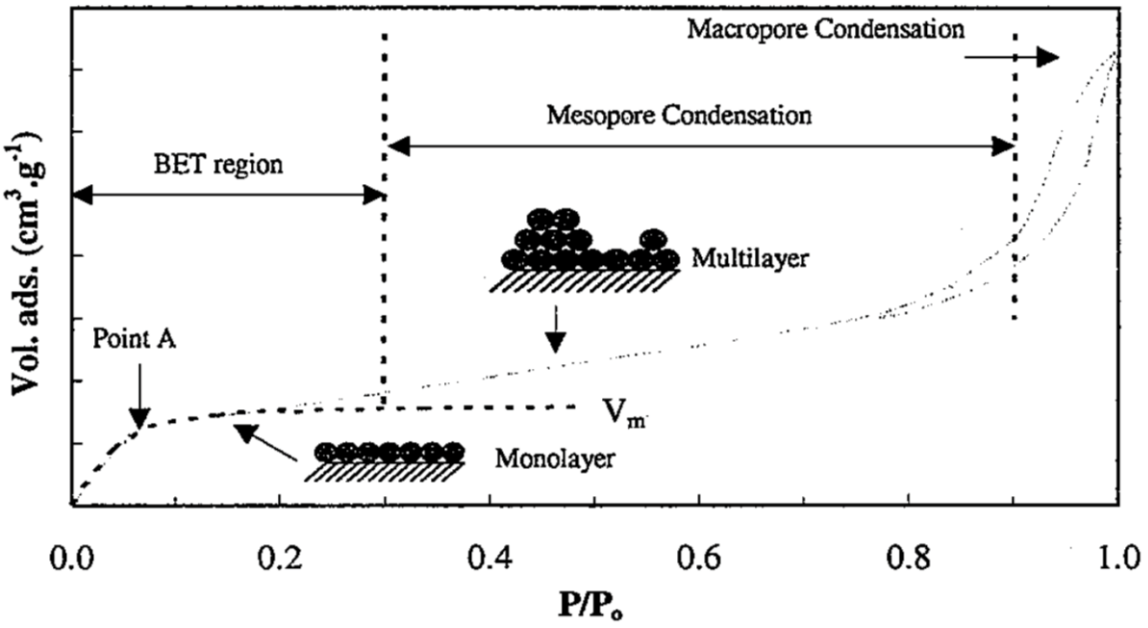

Figure 22. Typical isotherm for N_2 adsorption-desorption, originally from Macken, 1996. Figure modified from reference.[107]

DV optical emission spectrometer (PerkinElmer Corporation).

In this technique, the sample is subject to a high energy plasma source, to produce excited state atoms capable of emitting light (photons) as the electron moves to a less energetic energy level. Every element has its own unique electronic structure, meaning each electron will emit light at a set of wavelengths that is specific to each atomic ion. The intensity of a set of selected emission lines is linear to the amount of that element present. It is in this fashion that the elements present in the sample can be quantified.[106]

For sample preparation, approximately 5-10 mg of the sample would be weighed directly into a small volumetric flask, either 10 or 25 mL. For colloidal samples, the solvent would be evaporated directly from the volumetric flask before measurements were taken. Then, 1-2 mL of freshly prepared aqua regia (1:3 HNO_3:HCl) was inserted into the flask and heated at 75 °C for 30-60 minutes, depending on the nature of the sample. Finally, the flask would be diluted using 2% HNO_3 and filtered using a 0.45 μm pore filter. For each time the ICP-OES instrument was used, a calibration curve was attained by preparing 4 solutions for gold only compounds or 8 solutions for samples containing gold and another metal element. Calibration solutions were prepared for 0.5-5.0 ppm in 2% HCl for gold and 2% HNO_3 for other metals tested in this research using standard ICP solutions (1000 μg/mL, High-Purity Standards).

Scanning Transmission Electron Microscopy

STEM is a combination of TEM and SEM (scanning electron microscopy). Similar to TEM, STEM requires thin samples and looks at electron beams that have been transmitted by the sample. Like SEM, STEM has a very focused beam of electrons that scans across the sample in a raster pattern. The scattered signals are detected and then plotted as a property of the probe position, which in turn creates the magnified image.[108] Visual measurements were operated on Hitachi HD-2000 STEM and HAADF-STEM techniques with the aid of ImageJ. The samples were dispersed and diluted in ethanol or hexanes, depending on the

polarities of the sample, assisted by ultrasonic technique. Then, using a carbon film 300 mesh copper grid (3 mm), 1-2 drops of the diluted sample was placed onto the black carbon film side of the grid, and allowed to air dry for 15-30 minutes before being placed under vacuum for a minimum of 24 hours before being analyzed.

X-ray Photoelectron Spectroscopy

Oxidation states of the metals were determined via X-ray photoelectron spectroscopy (XPS). All XPS data was attained by ORNL staff member Harry Meyer using a Phi 5600LS instrument (Physical Electronics, Inc.), which utilized non-monochromatic Magnesium (Mg) K_α X-rays for analysis. Elemental analysis using XPS is able to determine elemental composition in the top several nm of a sample's surface, as well as identification of the chemical state of the elements present. The XPS instrument consists fundamentally of an X-ray source, extraction optics, energy filter, and a detector.[109] The Mg K_α X-rays interact with the atoms in the samples, which in turn emit a photoelectron; this is referred to the photoelectric effect. The kinetic energy (E_K) of the emitted electron is recorded and, in applying a conservation of energy equation with the spectrometer's work function (Φ), one can calculate the atomic binding energy (E_B) relative to the Fermi level of the sample (Equation 3).

$$E_B = h\mu - E_K - \phi \quad (3)$$

Fourier-Transform Infrared Radiation

To further investigate the core-shell structures, Fourier-transform infrared (FTIR) spectroscopy was utilized to analyze the CO adsorption behavior of the catalyst. In situ FTIR was ultimately used to obtain additional information about the dispersion and oxidation state of the Au in the sample. At 5 °C, 2% CO was flowed over the catalyst for 10 minutes before the spectrum was taken, while the spectral contribution from gaseous CO was subtracted. Then, the sample was purged with

2% Ar/He and spectra were taken after 3 and 10 minutes to determine how effectively the CO desorbed from the catalyst.

Characterization of Catalytic Activity

The catalytic activity of the core-shell structures was tested by analyzing its ability to oxidize CO to CO_2, as well as its ability to convert 2-propanol to acetone (via dehydrogenation) or propene (via dehydration). For the CO conversion tests, 20 mg of the $Au_{144}@Fe_2O_3$ catalyst was packed into a quartz tube (inner diameter = 4 mm), sealed on either side by quartz wool, a gas stream of 1% CO (balanced in air) flowed through the catalyst at a rate of 10 mL/min, and the exiting stream was analyzed by a gas chromatograph equipped with a dual molecular sieve/porous polymer column and a thermal conductivity detector. The reaction temperature was controlled using a voltage transformer attached to a furnace. In addition, FTIR spectroscopy was able to determine CO adsorption and desorption on the structure.

2-Propanol conversion was tested and experiments were conducted by Felipe Polo-Garzon at Oak Ridge National Laboratory (ORNL). Details of the steady-state kinetic measurements were similar to those reported on a recent publication,[110] and are described below.

> *"The conversion of 2-propanol was performed in an Altamira Instruments system (AMI-200). Each catalyst sample (30 mg, sieved to mesh 60-80) was diluted with quartz sand to minimize channeling and local temperature differences. The catalyst bed was placed inside a quartz u-tube and held in place by quartz wool at both ends of the bed. Each sample was pretreated under 50 mL/min of 5% O_2 in Ar or He at approximately 550 °C for 1 h. The temperature was lowered to around 300 °C, and the gas was switched to 50 mL/min of Ar. Liquid 2-propanol was fed into the system using a Chemyx Nexus 3000 syringe pump. All experiments were performed under conditions free of mass transfer limitations. Products were analyzed using a Buck Scientific Model 910 gas chromatograph (GC) equipped with a flame*

ionization detector and a Restek MXT-Q-BOND column. The GC response factor was calibrated employing 2-propanol as an internal standard and assuming a closed mass balance in the system. All lines were heated to avoid condensation. Each experiment was performed under differential conditions (conversion less than 17%) to determine activation energies. Thus, any effects of concentration and temperature gradients throughout the catalyst bed were minimized."[110]

CHAPTER FOUR

RESULTS AND DISCUSSION

Part of the information in this chapter is taken from Michelle Lukosi et al. paper, currently under editing.

$Au_{144}(SC_6H_{13})_{60}$ Nanocluster

The MALDI-TOF mass spectrum of the Au_{144} clusters with 1-hexanethiol capping is expected to show a broad peak at approximately 32,500 daltons (Da), calculated to be 35,397 Da (Figure 23A) and correlates very well with literature results (Figure 23B).[27] The peak position shift is due to partial loss and fragmentation of the thiol-gold (-RS-Au-SR-) staple motifs from the laser intensity under the MALDI conditions. Each $Au_{144}(SR)_{60}$ cluster has been previously calculated by other groups to have 30 staple motifs, which include 30 of the 144 Au atoms in the capping structure.[35] The broad peak shift from the MALDI spectra is easier to explain since each staple motif contributes ~430 Da to the total mass of the structure. For further characterization of these clusters, thin film XRD measurements were taken (Figure 24). The small broad peak, with FWHM being 5.16° 2θ and centered at 38.58° 2θ, indicates the Au cluster has a domain of approximately 1.7 nm in diameter, via the Scherrer equation (Equation 4).[100] This correlates well with DFT estimations of ~1.6 nm, calculated by another group.[35]

$$\frac{0.94 \times 0.1540598\ \text{nm}}{\left(5.16° \times \frac{\pi}{180}\right)\cos\left(\frac{38.58°}{2} \times \frac{\pi}{180}\right)} \cong 1.7\ \text{nm} \qquad (4)$$

$Au_{144}@Fe_2O_3$ Core-Shell Structure

Varied Shell Thickness

The thickness of the iron oxide shell was controlled by varying the amount of iron precursor added during the reaction. The different $Au_{144}@Fe_2O_3$ core-shell structures are referred to by their Au:Fe ratios by mass. The structures studied in

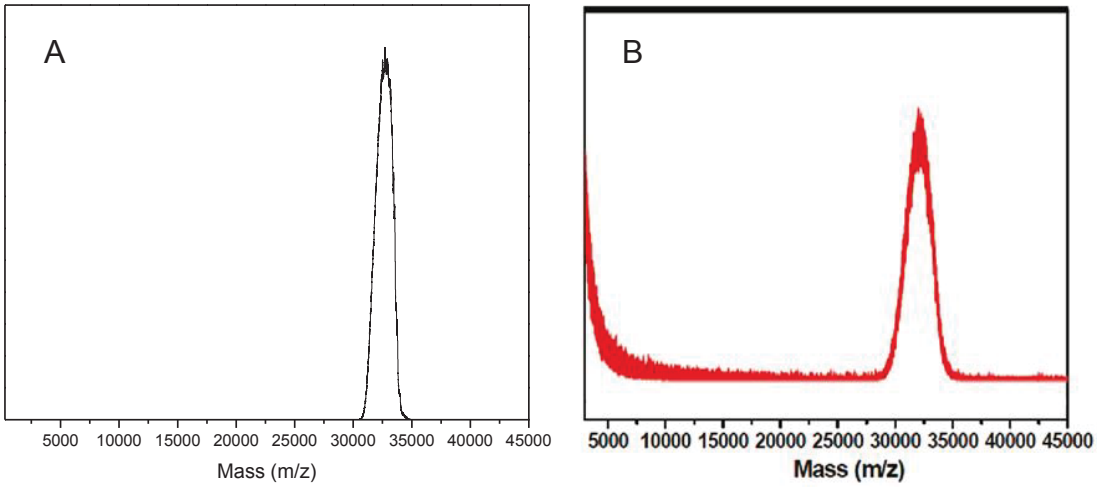

Figure 23. MALDI-TOF-MS of $Au_{144}(SC_6H_{13})_{60}$ with peak at 32,500 m/z (Da) A) experimental results vs B) literature results. Figure modified from reference[27]

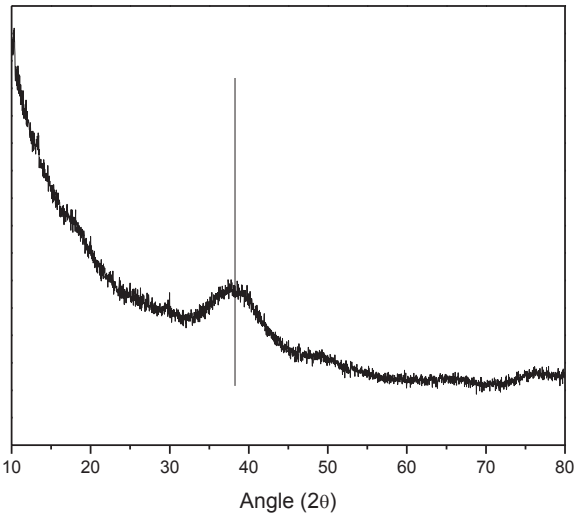

Figure 24. XRD of $Au_{144}(SC_6H_{13})_{60}$ thin film with broad peak at 38.58° 2θ indicative of small Au domain.

this paper were 1:2, 1:4, and 1:6. HAADF-STEM images of the 1:4 pre-loaded and, hence, pre-calcined, structures show a small Au_{144} particle surrounded by an iron oxide shell (Figure 25, more in the Appendix). There is a small gap at the core-shell interface, which is taken to be indicative of the thiol capping still attached to the gold cluster.

Once calcined to 300 °C, the thiol capping and other organic residuals, such as solvent surfactants that may still be in solution, are removed with the purpose of activating the gold catalysts. The structures that were fully covered reveal a yolk-shell like structure, rather than strictly a core-shell design (Figure 26B-C, more in the Appendix). This is due to the removal of thiol capping agent on the gold cluster, which winds up leaving a gap, or void, between the core and shell.

In my studies, a threshold limit was discovered for an optimal metal oxide shell of this particular morphology. When too little of the iron precursor ($Fe(CO)_5$) was added, the metal oxide was unable to cover the cluster completely, which led to sintering under calcination, as was the case with the 1:2 structure, and revealed a dumbbell-like structure (Figure 26A, more in the Appendix). The threshold amount may be different with a different thiol capping. For the 1:4 structure, the Fe_2O_3 shell was approximately 1.5 nm thick, while the 1:6 structure was approximately 2.5 nm thick, estimated via STEM. Surface area, via BET, was estimated to be larger for the 1:6 versus the 1:4 structure but they are relatively close (Table 2). This is believed to be because the 1:6 structures were not as uniform as the 1:4 structures due to some colloidal separation issues in the 1:6 structures. Isotherms of all the structures tested were shown to be Type IV isotherms (seen in the Appendix), which is indicative of limited multilayer formation.

Bulk gold has a face-centered-cubic (fcc) crystal structure, and when analyzed with XRD, there will be a predominant peak at 38.2° 2θ and less predominant peaks at 44.4°, 64.5°, and 77.5° 2θ representing the (111), (200), (220), and (311) surface planes, respectively, (Joint Committee on Powder Diffraction Standards-International Center for Diffraction Data (JCPDS-ICDD) file #04-0784). However, very small particles (<2 nm) can be quite difficult to detect

Table 2. BET surface area and ICP-OES weight percent of core-shell structure loaded onto silica.

Sample	SA_{BET} (m^2/g)	Au_{ICP} (wt %)	Fe_{ICP} (wt %)
SiO_2	355.9	-	-
Fe_2O_3/SiO_2	181.5	-	2.3
Au_{144}/SiO_2	182.1	1.4	-
1:2 $Au_{144}@Fe_2O_3/SiO_2$	136.1	1.2	5.8
1:4 $Au_{144}@Fe_2O_3/SiO_2$	164.6	1.2	4.8
1:6 $Au_{144}@Fe_2O_3/SiO_2$	171.6	1.5	9.2

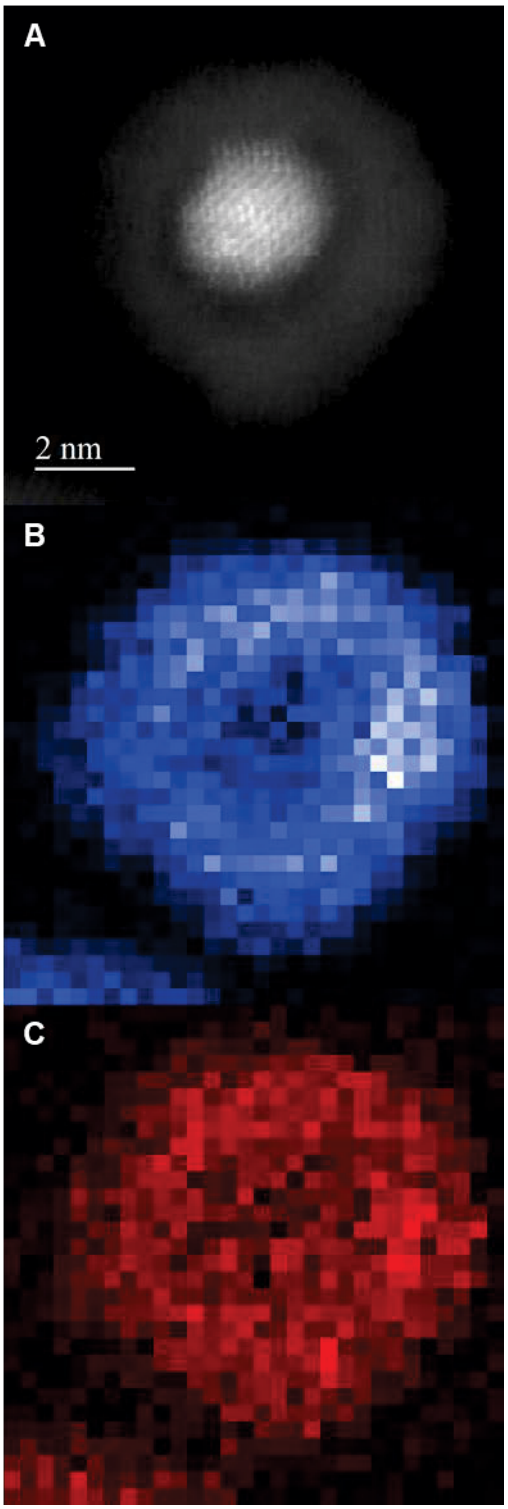

Figure 25. A) HAADF-STEM of 1:4 Au_{144}@Fe_2O_3 structure as synthesized, as well as the B) Fe (blue) and C) O (red) areal density of the structure.

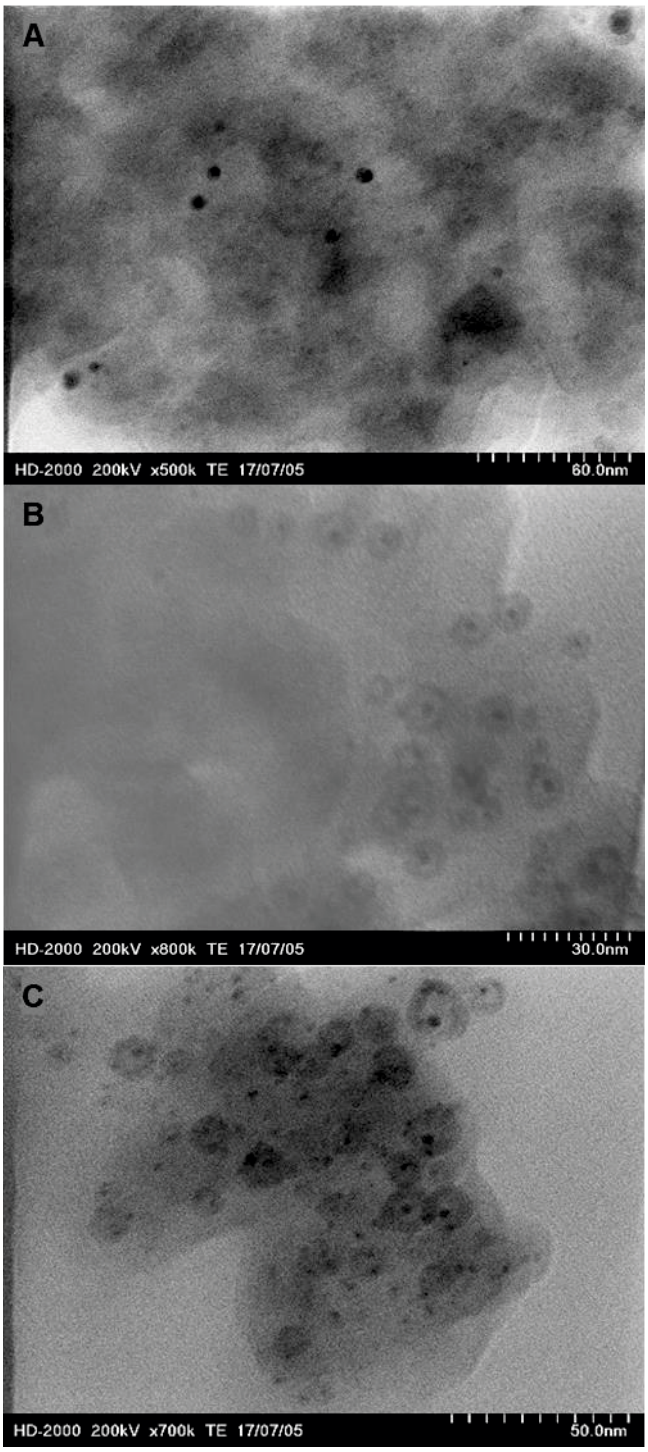

Figure 26. STEM of Au_{144}@Fe_2O_3/SiO_2 with varying Fe_2O_3 content for the A) 1:2, B) 1:4, and C) 1:6 structures.

and XRD is no exception.[111] Some other factors to consider in these measurements is that the iron oxide shell is amorphous in nature, as well as the weight fraction of gold being very small. With the Au_{144} clusters, there is barely a hump at the prominent angle at 38° 2θ, with the exception of the 1:2 structure (Figure 27). After calcination, it is clear that the 1:2 structures sintered as that peak becomes sharper and more defined, representative of larger gold particles. This corroborates the STEM images above, that the iron oxide shell was unable to cover the particle completely and, without the protective shell, the Au_{144} clusters coalesced. For the 1:4 and 1:6 structures, no sintering was visible from the XRD spectra, which is indicative of full coverage by the amorphous iron oxide shell, as the STEM images indicate.

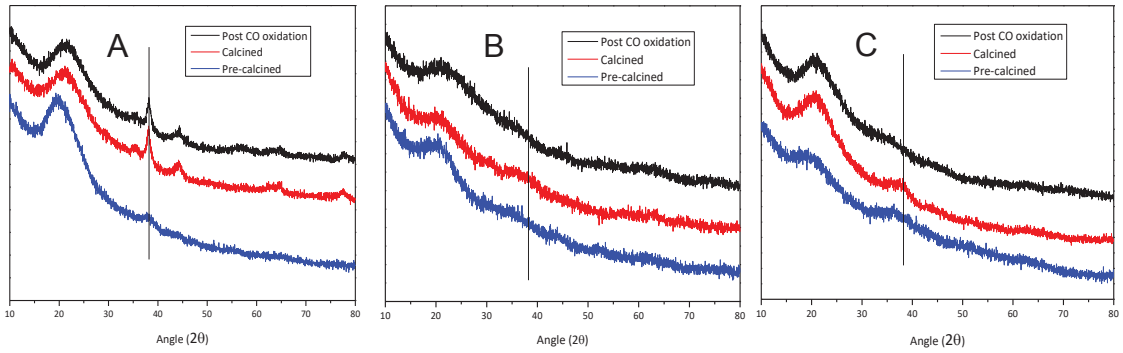

Figure 27. XRD of $Au_{144}@Fe_2O_3/SiO_2$ with varying Fe_2O_3 content for A) 1:2, B) 1:4, and C) 1:6 structures, with a line at 38.2° 2θ where bulk gold peaks are prominent.

XPS of the 1:4 structure, which was loaded onto fumed silica and calcined at 300 °C, provided a survey spectrum, or wide-scan showing all elements present, (Figure 28A) with subsequent high resolution (core level) spectra of each element identified (Figure 28B-F), as well as the overall percentage surface composition that each element contributes (Table 3). The peak width, for gold, is very broad, which is characteristic of a very small particle. There is a slight shift of -0.2 eV in the binding energy for the Au $4f_{7/2}$ peak from 84.0 eV that is typically seen for bulk

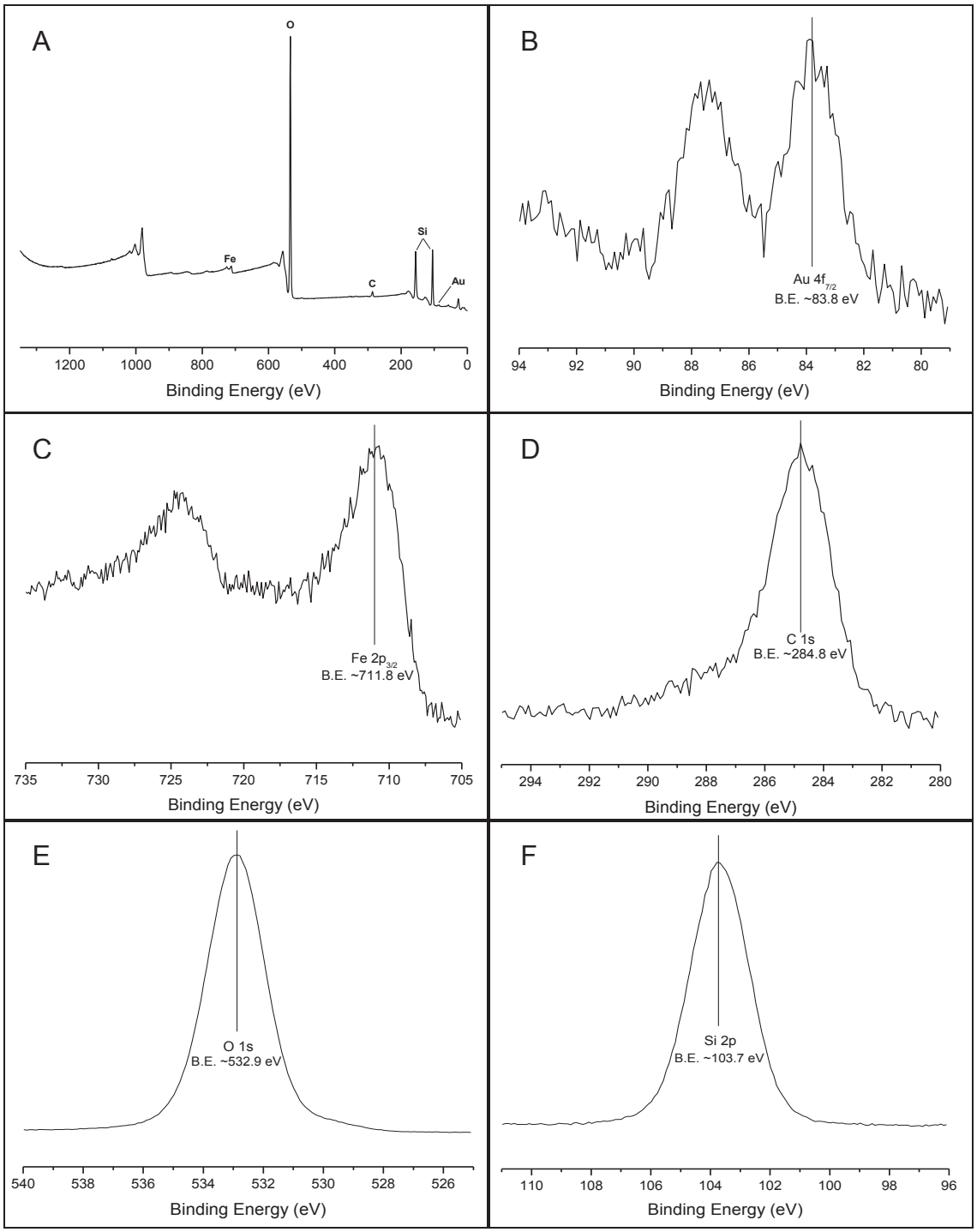

Figure 28. XPS of surface composition of $Au_{144}@Fe_2O_3/SiO_2$ 1:4 structure showing A) the survey spectrum and the high-resolution spectra of B) gold, C) iron, D) oxygen, E) silicon, and F) carbon.

gold. This shift may be due to the iron oxide layer that covers the gold cluster, providing a slight addition to the gold atom's valence electron charge. The Fe $2p_{3/2}$ peak shows a primary 3^+ valence, which means the iron oxide shell is in the Fe_2O_3 structure. The O 1s orbital is primarily associated with the Si 2p orbital from the SiO_2 support. The C 1s signal was relatively low and is predominantly adsorbed carbonaceous material during analysis.

Table 3. XPS – Surface Composition (at.%): $Au_{144}@Fe_2O_3/SiO_2$.

Au	Fe	Si	O	C	Na
0.06	1.12	31.49	63.17	3.85	0.31

Synergistic effects of core-shell system

CO Oxidation

Using control experiments of Au_{144} NCs and Fe_2O_3 NPs loaded onto silica, (Au_{144}/SiO_2 and Fe_2O_3/SiO_2, respectively) I was able to compare with the $Au_{144}@Fe_2O_3/SiO_2$ core-shell particles. Using CO oxidation tests, the synergistic effects of the core-shell structures are apparent by comparison of each structures catalytic abilities (Figure 29). For the core-shell structures, full oxidation of CO for the 1:2, 1:4, and 1:6 structures occurred at 211, 75, and 111 °C, respectively. Au_{144} NCs by themselves showed some oxidation at room temperature, but did not exhibit full oxidation of CO until ~500 °C. Whereas, Fe_2O_3 NPs by themselves never reached full CO oxidation, up to 500 °C. The Au_{144} NCs were determined to have sintered into larger particles, and more evidence that sintering occurred was that the catalyzed Au_{144} particles visibly appeared a red/purple color after testing was completed.

To further investigate the behavior of CO adsorption onto the $Au_{144}@Fe_2O_3$ particle and obtain more information about the Fe_2O_3 surface, FTIR spectroscopy of the 1:4 core-shell structure, loaded onto fumed silica and calcined at 300 °C,

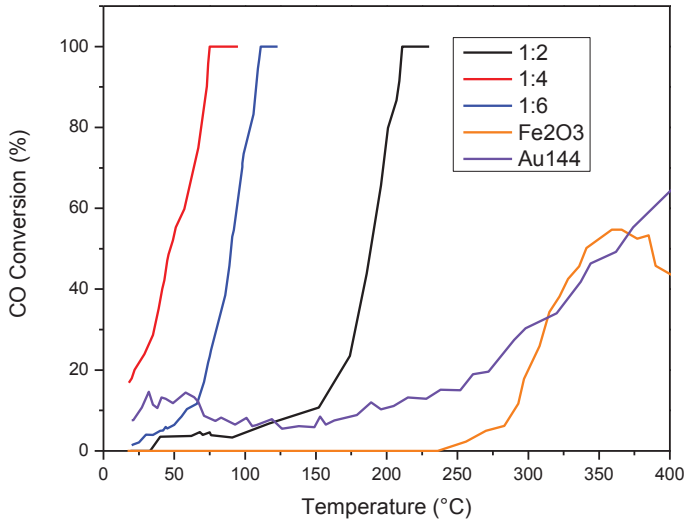

Figure 29. CO conversion on $Au_{144}@Fe_2O_3/SiO_2$ catalysts with varying Fe_2O_3 shell thickness, as well as Au_{144}/SiO_2 and Fe_2O_3/SiO_2.

was obtained at 5 °C (Figure 30). The top spectrum was taken after 10 minutes of 2% CO flow, with any spectral contribution from gaseous CO subtracted. The middle and bottom spectra were taken after purging the sample with 2% He for 3 and 10 minutes, respectively. There was only one distinct peak at 2139 cm^{-1}, from the top spectrum, which can be attributed to CO being adsorbed onto a positively charged Au species ($Au^{\delta+}$, $0 < \delta < 1$).[112-113] The middle and bottom spectra showed no distinct peaks, which signifies that the CO was readily desorbed from the catalyst surface. The positively charged Au species is attributed to the iron oxide layer that is surrounding the Au core.

2-Propanol Conversion

Control studies of Au_{144}/SiO_2 and Fe_2O_3/SiO_2, with 1.4% Au and 2.3% Fe (Table 4), respectively, loaded onto a fumed silica substrate were used for comparison to the core-shell counterpart. From the previous study with CO oxidation, the 1:4 Au:Fe by mass ratio structure of $Au_{144}@Fe_2O_3/SiO_2$ was shown to have the best catalytic activity. Therefore, the conversion of 2-propanol was tested exclusively on those structures. With 1.2% Au loading, the data suggests that the core-shell structure has a synergistic effect on the acetone and propene production (Figure 31).Further, the core-shell structure provides intermediate selectivity for the reaction products, when compared with the supported catalysts. This suggests that the core-shell structure has the potential for tailoring reaction selectivity (Figure 32A-B). However, the synergy of this core-shell structure is not yet conclusive until reaction rates per active site are obtained, which requires further characterization under reaction conditions. In Figure 31C, selectivity towards an unknown compound is observed at low conversions. Diisopropyl ether has already been ruled out as a possibility for the unknown product and it is more than likely a coupling product and is not considered to study the acid-base properties of the material.

Thermal Treatments of 1:4 $Au_{144}@Fe_2O_3$ Structure

The 1:4 structure, with the best CO oxidation results, was put through varying thermal treatments to test the structure's optimal activity. The structure was tested at pretreatments of 300, 500, and 700 °C. Results for the 300 °C

Table 4. 2-Propanol conversion activation energies (E_{act}).

Catalyst Loaded onto Silica	Loading (%)		E_{act} global (kJ/mol)	E_{act} propene (kJ/mol)	E_{act} acetone (kJ/mol)
	Au	Fe			
Fe_2O_3	-	2.3	92	71	136
Au_{144}	1.4	-	74	-	79
1:4 $Au_{144}@Fe_2O_3$	1.2	4.8	90	105	99

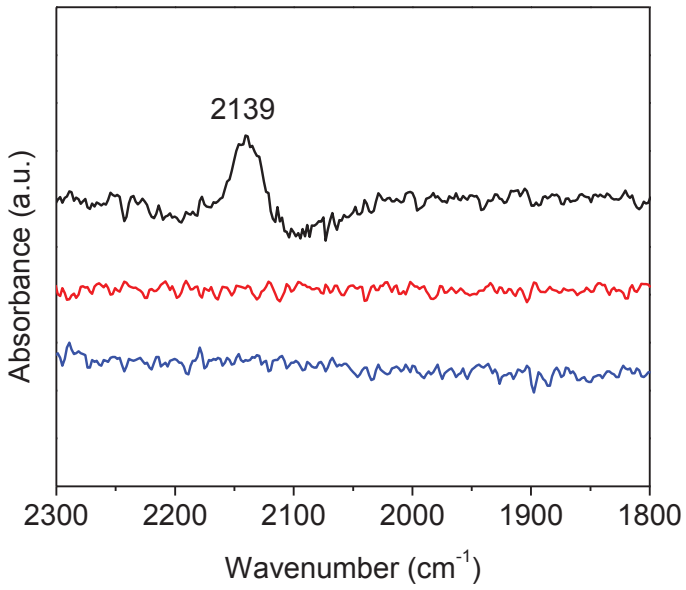

Figure 30. FTIR of CO adsorption onto 1:4 structure $Au_{144}@Fe_2O_3/SiO_2$ at 5 °C (gaseous CO contribution subtracted).

pretreatments showed the best activity with full conversion at 75 °C (Figure 33A). It should be noted, however, that the 1:4 structure showed full conversion at 95 °C for both pretreatments at 500 and 700 °C. Although the higher temperature pretreatments do not display the best catalytic activity, it is still active below 100 °C, which is more efficient than the 1:6 structure pretreated at 300 °C. This indicates thermal stability at these higher calcination temperatures. Even with a thin shell, as long as full coverage of the core is apparent, the small Au cluster can remain relatively stabilized. However, the XRD for these 1:4 samples (Figure 33B) shows some sintering as the pretreatment temperature is increased, where the peaks become more defined, particularly at 38.2° 2θ, where bulk gold is typically represented.

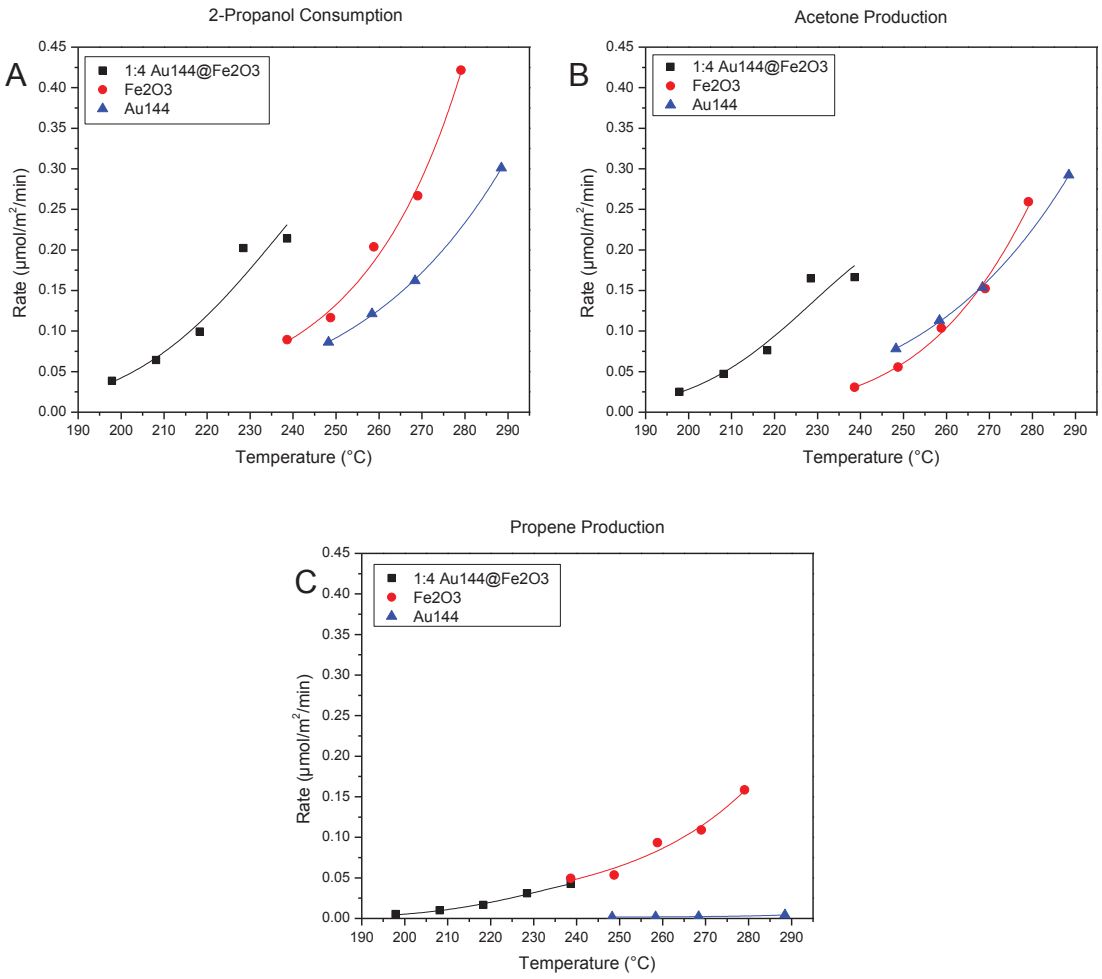

Figure 31. 2-Propanol conversion reactions showing A) 2-propanol consumption rates, B) acetone production rates, and C) propene production rates.

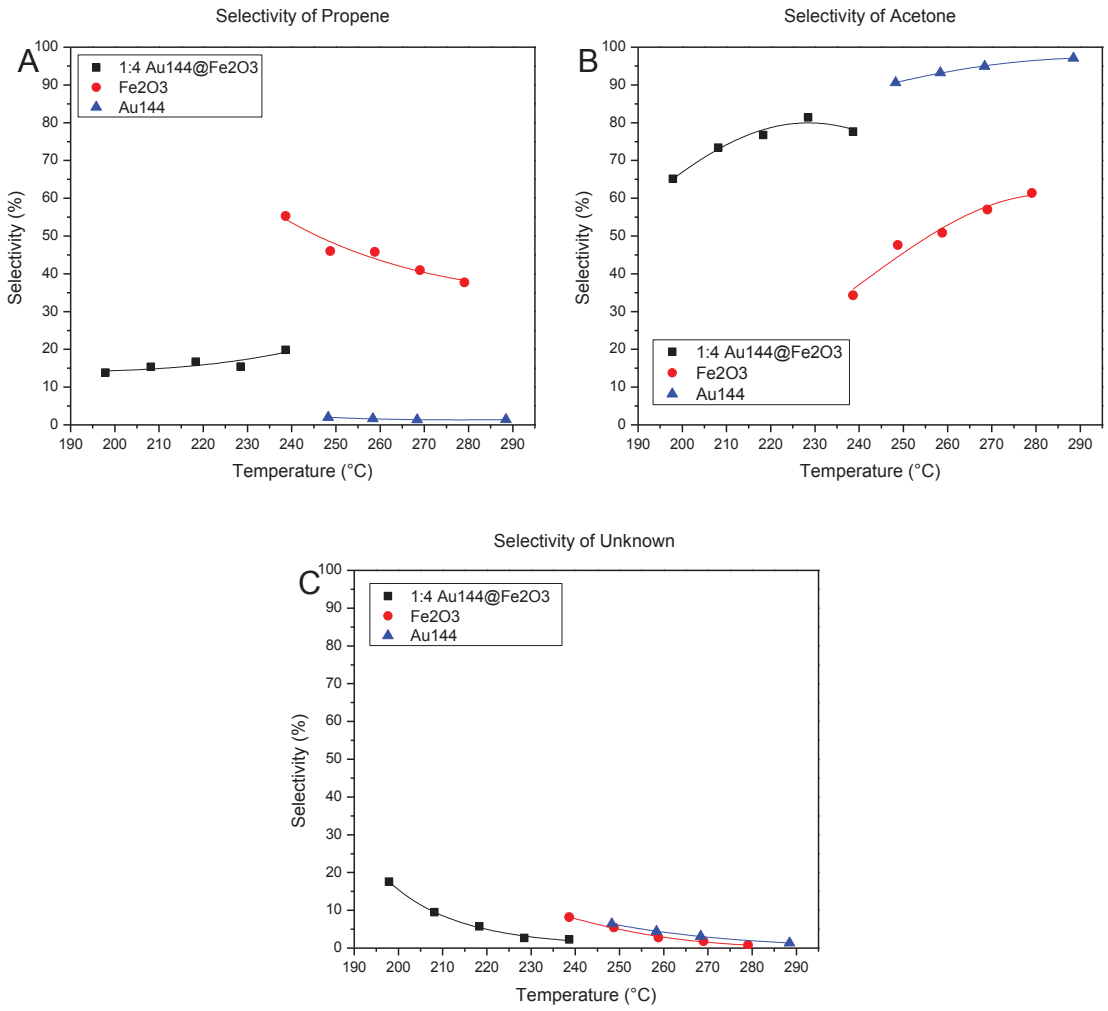

Figure 32. 2-Propanol conversion reactions showing selectivity to A) propene, B) acetone, and C) of an unknown compound.

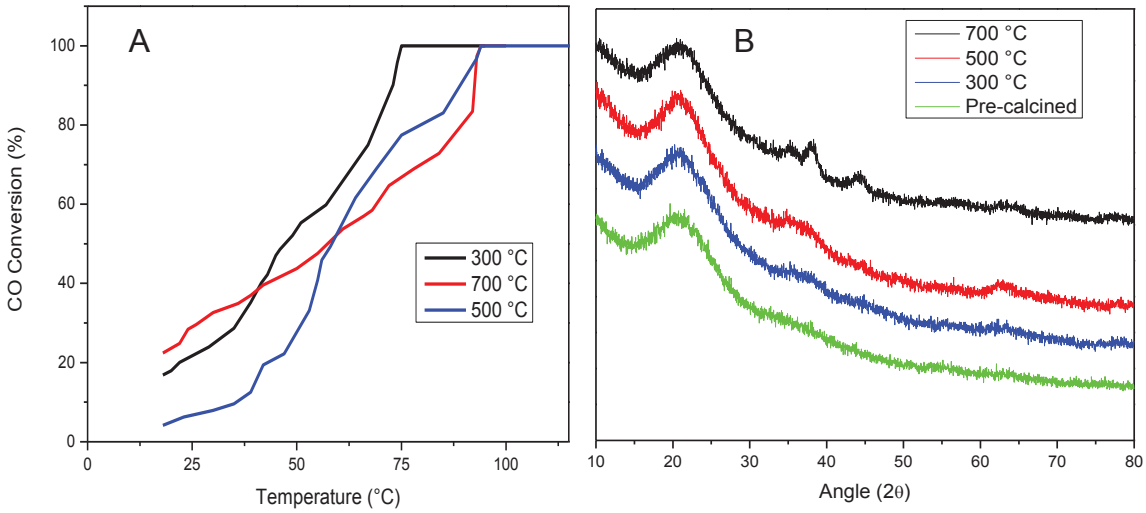

Figure 33. The 1:4 Au_{144}@Fe_2O_3/SiO_2 structure calcined at temperatures 300, 500 & 700 °C showing A) CO conversion and B) XRD spectra.

CHAPTER FIVE
RESEARCH CONCLUSIONS

$Au_{144}@Fe_2O_3$ Core-Shell Structure

$Au_{144}@Fe_2O_3$ core-shell structures were synthesized with varying shell thickness by varying the metal oxide precursor used. These structures were loaded onto a fumed silica support via colloidal deposition, calcined at 300 °C, and the structure's catalytic activities were compared based on the efficiency of CO oxidation. Between the $Au_{144}@Fe_2O_3/SiO_2$ 1:2, 1:4, and 1:6 core-shell structures, the 1:4 structure exhibited 100% oxidation of CO at the lowest temperature, 75 °C, and the 1:6 structure, with a thicker iron oxide shell, reached full oxidation of CO at a slightly higher temperature, 111 °C. The 1:2 structure did not result in full core coverage, which is why it exhibited poor CO oxidation properties compared to the 1:4 and 1:6 structures and represents a minimum threshold of Fe_2O_3 shell thickness. Based on these results, the 1:4 structure was studied under thermal treatments of 300, 500, and 700 °C, followed by CO oxidation. The results showed that the best results for the 1:4 structure was at 300 °C pretreatment, however, higher temperature pretreatments still showed promising results with full CO conversion below 100 °C. 2-Propanol conversion results adumbrate that there is a synergistic effect of the 1:4 core-shell structure over the non-encapsulated counterparts. However, this claim cannot be made until the rates are calculated per active site (TOF) instead of per surface area. A normalized comparison could be made if the size of the particles for each catalyst is obtained and the wetting of the particles on the support is similar for all cases.

Future Directions

The first step is to complete the 2-propanol conversion analyses for the other two $Au_{144}@Fe_2O_3$ core-shell structures mentioned in this research, 1:2 and 1:6. Some of the next steps that are intended to be followed are the continued study of these gold cluster-metal oxide core-shell structures with different metal

oxide shells, while attempting to control shell thickness and stability to improve catalytic activity. One such method is to use similar transition metal carbonyl complexes, such as dicobalt octacarbonyl and dimanganese decacarbonyl. Another avenue is to use a combination of iron, manganese, and/or cobalt precursors in order to synthesize a gold cluster core with an alloy oxide shell. Another study is to synthesize the same structures using a different gold cluster. The Au_{25} nanocluster is currently being investigated by another colleague at this time.

REFERENCES

1. Ibrahim, A. A. E.-M., *Pictured Glossary in Biology*. Scientific Research Publishing, Inc. USA: 2017.
2. Laidler, K. J.; Cornish-Bowden, A., Elizabeth Fulhame and the discovery of catalysis: 100 years before Buchner. *Cornish-Bowden (1997) pp* **1997**, 123-126.
3. Cornish-Bowden, A., Two centuries of catalysis. *J. Biosci.* **1998,** *23* (2), 87-92.
4. Laidler, K. J., The development of theories of catalysis. *Archive for history of exact sciences* **1986,** *35* (4), 345-374.
5. Bond, G. C.; Louis, C.; Thompson, D. T., *Catalysis by gold*. World Scientific: 2006; Vol. 6.
6. Sinthika, S.; Vala, S. T.; Kawazoe, Y.; Thapa, R., CO Oxidation Prefers the Eley–Rideal or Langmuir–Hinshelwood Pathway: Monolayer vs Thin Film of SiC. *ACS Appl. Mater. Interfaces* **2016,** *8* (8), 5290-5299.
7. Herbschleb, C. T., *ReactorSTM: imaging catalysts under realistic conditions*. Faculty of Science, Leiden University: 2011.
8. Haruta, M.; Kobayashi, T.; Sano, H.; Yamada, N., Novel gold catalysts for the oxidation of carbon monoxide at a temperature far below 0. DEG. C. *Chem. Lett.* **1987,** *16* (2), 405-408.
9. Hutchings, G. J.; Haruta, M., A golden age of catalysis: A perspective. *Applied Catalysis A: General* **2005,** *291* (1), 2-5.
10. Haruta, M., Chance and necessity: my encounter with gold catalysts. *Angew. Chem. Int. Ed.* **2014,** *53* (1), 52-56.
11. Bond, G. C., The effect of the metal to non-metal transition on the activity of gold catalysts. *Faraday Discuss.* **2011,** *152*, 277-291.
12. Haruta, M., When gold is not noble: catalysis by nanoparticles. *The Chemical Record* **2003,** *3* (2), 75-87.
13. Valden, M.; Lai, X.; Goodman, D. W., Onset of catalytic activity of gold clusters on titania with the appearance of nonmetallic properties. *Science* **1998,** *281* (5383), 1647-1650.
14. Haruta, M., Spiers memorial lecture role of perimeter interfaces in catalysis by gold nanoparticles. *Faraday Discuss.* **2011,** *152*, 11-32.
15. Wang, L.; Zhang, B.; Zhang, W.; Zhang, J.; Gao, X.; Meng, X.; Su, D. S.; Xiao, F.-S., Positively charged bulk Au particles as an efficient catalyst for oxidation of styrene with molecular oxygen. *Chem. Commun.* **2013,** *49* (33), 3449-3451.
16. Harkness, K. M.; Fenn, L. S.; Cliffel, D. E.; McLean, J. A., Surface fragmentation of complexes from thiolate protected gold nanoparticles by ion mobility-mass spectrometry. *Anal. Chem.* **2010,** *82* (7), 3061-3066.
17. Guzman, J.; Gates, B. C., Simultaneous presence of cationic and reduced gold in functioning MgO-supported CO oxidation catalysts: Evidence from X-ray absorption spectroscopy. *J. Phys. Chem. B* **2002,** *106* (31), 7659-7665.

18. Boccuzzi, F.; Chiorino, A.; Manzoli, M.; Lu, P.; Akita, T.; Ichikawa, S.; Haruta, M., Au/TiO 2 nanosized samples: a catalytic, TEM, and FTIR study of the effect of calcination temperature on the CO oxidation. *J. Catal.* **2001,** *202* (2), 256-267.
19. Haruta, M., Gold as a novel catalyst in the 21st century: Preparation, working mechanism and applications. *Gold Bulletin* **2004,** *37* (1), 27-36.
20. Lukosi, M.; Zhu, H.; Dai, S., Recent advances in gold-metal oxide core-shell nanoparticles: Synthesis, characterization, and their application for heterogeneous catalysis. *Frontiers of Chemical Science and Engineering* **2016,** *10* (1), 39-56.
21. Arcidiacono, S.; Bieri, N.; Poulikakos, D.; Grigoropoulos, C., On the coalescence of gold nanoparticles. *Int. J. Multiphase Flow* **2004,** *30* (7), 979-994.
22. Golunski, S., Why use platinum in catalytic converters? *Tc* **2007,** *975*, 44.
23. Brust, M.; Walker, M.; Bethell, D.; Schiffrin, D. J.; Whyman, R., Synthesis of thiol-derivatised gold nanoparticles in a two-phase liquid–liquid system. *J. Chem. Soc., Chem. Commun.* **1994,** (7), 801-802.
24. Chen, T.; Luo, Z.; Yao, Q.; Yeo, A. X. H.; Xie, J., Synthesis of thiolate-protected Au nanoparticles revisited: U-shape trend between the size of nanoparticles and thiol-to-Au ratio. *Chemical Communications* **2016,** *52* (61), 9522-9525.
25. Azubel, M.; Kornberg, R. D., Synthesis of Water-Soluble, Thiolate-Protected Gold Nanoparticles Uniform in Size. *Nano letters* **2016,** *16* (5), 3348-3351.
26. Schmid, G.; Fenske, D., Metal clusters and nanoparticles. *Philosophical Transactions of the Royal Society of London A: Mathematical, Physical and Engineering Sciences* **2010,** *368* (1915), 1207-1210.
27. Qian, H.; Jin, R., Ambient synthesis of Au144 (SR) 60 nanoclusters in methanol. *Chem. Mater.* **2011,** *23* (8), 2209-2217.
28. Chaki, N. K.; Negishi, Y.; Tsunoyama, H.; Shichibu, Y.; Tsukuda, T., Ubiquitous 8 and 29 kDa gold: alkanethiolate cluster compounds: mass-spectrometric determination of molecular formulas and structural implications. *J. Am. Chem. Soc.* **2008,** *130* (27), 8608-8610.
29. Jin, R.; Qian, H.; Wu, Z.; Zhu, Y.; Zhu, M.; Mohanty, A.; Garg, N., Size focusing: a methodology for synthesizing atomically precise gold nanoclusters. *J. Phys. Chem. Lett.* **2010,** *1* (19), 2903-2910.
30. Liu, J.; Jian, N.; Ornelas, I.; Pattison, A. J.; Lahtinen, T.; Salorinne, K.; Häkkinen, H.; Palmer, R. E., Exploring the atomic structure of 1.8 nm monolayer-protected gold clusters with aberration-corrected STEM. *Ultramicroscopy* **2017,** *176*, 146-150.
31. Guryanov, I.; Polo, F.; Ubyvovk, E. V.; Korzhikova-Vlakh, E.; Tennikova, T.; Rad, A. T.; Nieh, M.-P.; Maran, F., Polylysine-grafted Au 144 nanoclusters: birth and growth of a healthy surface-plasmon-resonance-like band. *Chemical Science* **2017,** *8* (4), 3228-3238.

32. Qian, H.; Zhu, M.; Wu, Z.; Jin, R., Quantum sized gold nanoclusters with atomic precision. *Acc. Chem. Res.* **2012,** *45* (9), 1470-1479.
33. Bahena, D.; Bhattarai, N.; Santiago, U.; Tlahuice, A.; Ponce, A.; Bach, S. B.; Yoon, B.; Whetten, R. L.; Landman, U.; Jose-Yacaman, M., STEM electron diffraction and high-resolution images used in the determination of the crystal structure of the Au144 (SR) 60 cluster. *J. Phys. Chem. Lett.* **2013,** *4* (6), 975-981.
34. MacDonald, M. A.; Zhang, P.; Qian, H.; Jin, R., Site-Specific and Size-Dependent Bonding of Compositionally Precise Gold− Thiolate Nanoparticles from X-ray Spectroscopy. *J. Phys. Chem. Lett.* **2010,** *1* (12), 1821-1825.
35. Weissker, H.-C.; Escobar, H. B.; Thanthirige, V.; Kwak, K.; Lee, D.; Ramakrishna, G.; Whetten, R.; López-Lozano, X., Information on quantum states pervades the visible spectrum of the ubiquitous Au144 (SR) 60 gold nanocluster. *Nature communications* **2014,** *5*.
36. Haruta, M., Catalysis of gold nanoparticles deposited on metal oxides. *Cattech* **2002,** *6* (3), 102-115.
37. Hill, A. F., *Organotransition metal chemistry*. Royal Society of Chemistry: 2002; Vol. 7.
38. Huang, H.; Wang, X., Recent progress on carbon-based support materials for electrocatalysts of direct methanol fuel cells. *J. Mater. Chem. A* **2014,** *2* (18), 6266-6291.
39. Lin, F.-h.; Doong, R.-a., Bifunctional Au− Fe3O4 heterostructures for magnetically recyclable catalysis of nitrophenol reduction. *J. Phys. Chem. C* **2011,** *115* (14), 6591-6598.
40. Yin, H.; Ma, Z.; Chi, M.; Dai, S., Heterostructured catalysts prepared by dispersing Au@ Fe 2 O 3 core–shell structures on supports and their performance in CO oxidation. *Catal. Today* **2011,** *160* (1), 87-95.
41. Zhuang, Z.; Sheng, W.; Yan, Y., Synthesis of Monodispere Au@ Co3O4 Core-Shell Nanocrystals and Their Enhanced Catalytic Activity for Oxygen Evolution Reaction. *Adv. Mater.* **2014,** *26* (23), 3950-3955.
42. Tripathy, S. K.; Mishra, A.; Jha, S. K.; Wahab, R.; Al-Khedhairy, A. A., Synthesis of thermally stable monodispersed Au@ SnO 2 core–shell structure nanoparticles by a sonochemical technique for detection and degradation of acetaldehyde. *Analytical Methods* **2013,** *5* (6), 1456-1462.
43. Janardhanan, V. M.; Deutschmann, O., CFD analysis of a solid oxide fuel cell with internal reforming: Coupled interactions of transport, heterogeneous catalysis and electrochemical processes. *J. Power Sources* **2006,** *162* (2), 1192-1202.
44. Zhu, H.; Sigdel, A.; Zhang, S.; Su, D.; Xi, Z.; Li, Q.; Sun, S., Core/Shell Au/MnO Nanoparticles Prepared Through Controlled Oxidation of AuMn as an Electrocatalyst for Sensitive H2O2 Detection. *Angew. Chem.* **2014,** *126* (46), 12716-12720.
45. Zhu, Z.; Chang, J.-L.; Wu, R.-J., Fast ozone detection by using a core–shell Au@ TiO 2 sensor at room temperature. *Sensors and Actuators B: Chemical* **2015,** *214*, 56-62.

46. Mitsudome, T.; Yamamoto, M.; Maeno, Z.; Mizugaki, T.; Jitsukawa, K.; Kaneda, K., One-step Synthesis of Core-Gold/Shell-Ceria Nano-material and Its Catalysis for Highly Selective Semihydrogenation of Alkynes. *J. Am. Chem. Soc.* **2015**.
47. Wei, Y.; Zhao, Z.; Yu, X.; Jin, B.; Liu, J.; Xu, C.; Duan, A.; Jiang, G.; Ma, S., One-pot synthesis of core–shell Au@ CeO 2− δ nanoparticles supported on three-dimensionally ordered macroporous ZrO 2 with enhanced catalytic activity and stability for soot combustion. *Catalysis Science & Technology* **2013,** *3* (11), 2958-2970.
48. Liu, J.; Jiang, J.; Cheng, C.; Li, H.; Zhang, J.; Gong, H.; Fan, H. J., Co3O4 Nanowire@MnO2 Ultrathin Nanosheet Core/Shell Arrays: A New Class of High-Performance Pseudocapacitive Materials. *Adv. Mater.* **2011,** *23* (18), 2076-2081.
49. Wu, X.-F.; Chen, Y.-F.; Yoon, J.-M.; Yu, Y.-T., Fabrication and properties of flower-shaped Pt@ TiO 2 core–shell nanoparticles. *Mater. Lett.* **2010,** *64* (20), 2208-2210.
50. Tauster, S., Strong metal-support interactions. *Acc. Chem. Res.* **1987,** *20* (11), 389-394.
51. Zhang, J.; Tang, Y.; Lee, K.; Ouyang, M., Tailoring light-matter-spin interactions in colloidal hetero-nanostructures. *Nature* **2010,** *466* (7302), 91-95.
52. Alivisatos, A. P., Semiconductor clusters, nanocrystals, and quantum dots. *Science* **1996,** *271* (5251), 933-937.
53. Baker, G. A., Nanoparticles: From Theory to Application Edited by Günter Schmid (University of Duisberg-Essen). Wiley-VCH Verlag GmbH & Co. KGaA: Weinheim, Germany. 2004. x+ 434 pp. $210.00. ISBN 3-527-30507-6. *J. Am. Chem. Soc.* **2004,** *126* (47), 15632-15633.
54. Aguirre, M. E.; Rodríguez, H. B.; San Román, E.; Feldhoff, A.; Grela, M. A., Ag@ ZnO core–shell nanoparticles formed by the timely reduction of Ag+ ions and zinc acetate hydrolysis in N, N-dimethylformamide: mechanism of growth and photocatalytic properties. *J. Phys. Chem. C* **2011,** *115* (50), 24967-24974.
55. Arroyo-Ramírez, L.; Chen, C.; Cargnello, M.; Murray, C. B.; Fornasiero, P.; Gorte, R. J., Supported platinum–zinc oxide core–shell nanoparticle catalysts for methanol steam reforming. *J. Mater. Chem. A* **2014,** *2* (45), 19509-19514.
56. Zhang, N.; Liu, S.; Fu, X.; Xu, Y.-J., Synthesis of M@ TiO2 (M= Au, Pd, Pt) core–shell nanocomposites with tunable photoreactivity. *J. Phys. Chem. C* **2011,** *115* (18), 9136-9145.
57. An, K.; Zhang, Q.; Alayoglu, S.; Musselwhite, N.; Shin, J.-Y.; Somorjai, G. A., High-Temperature Catalytic Reforming of n-Hexane over Supported and Core–Shell Pt Nanoparticle Catalysts: Role of Oxide–Metal Interface and Thermal Stability. *Nano Lett.* **2014,** *14* (8), 4907-4912.
58. Liu, S.; Xie, M.; Li, Y.; Guo, X.; Ji, W.; Ding, W.; Au, C., Novel sea urchin-like hollow core–shell SnO 2 superstructures: facile synthesis and excellent ethanol sensing performance. *Sensors and Actuators B: Chemical* **2010,** *151* (1), 229-235.

59. Phadungdhitidhada, S.; Thanasanvorakun, S.; Mangkorntong, P.; Choopun, S.; Mangkorntong, N.; Wongratanaphisan, D., SnO 2 nanowires mixed nanodendrites for high ethanol sensor response. *Current Applied Physics* **2011,** *11* (6), 1368-1373.
60. McAleer, J. F.; Moseley, P. T.; Norris, J. O.; Williams, D. E., Tin dioxide gas sensors. Part 1.—Aspects of the surface chemistry revealed by electrical conductance variations. *Journal of the Chemical Society, Faraday Transactions 1: Physical Chemistry in Condensed Phases* **1987,** *83* (4), 1323-1346.
61. Yu, K.; Wu, Z.; Zhao, Q.; Li, B.; Xie, Y., High-temperature-stable Au@ SnO2 core/shell supported catalyst for CO oxidation. *J. Phys. Chem. C* **2008,** *112* (7), 2244-2247.
62. Galeano, C.; Güttel, R.; Paul, M.; Arnal, P.; Lu, A. H.; Schüth, F., Yolk-Shell Gold Nanoparticles as Model Materials for Support-Effect Studies in Heterogeneous Catalysis: Au,@ C and Au,@ ZrO2 for CO Oxidation as an Example. *Chem. Eur. J.* **2011,** *17* (30), 8434-8439.
63. Bakhmutsky, K.; Wieder, N. L.; Cargnello, M.; Galloway, B.; Fornasiero, P.; Gorte, R. J., A Versatile Route to Core–Shell Catalysts: Synthesis of Dispersible M@ Oxide (M= Pd, Pt; Oxide= TiO2, ZrO2) Nanostructures by Self-Assembly. *ChemSusChem* **2012,** *5* (1), 140-148.
64. Manicone, P. F.; Iommetti, P. R.; Raffaelli, L., An overview of zirconia ceramics: basic properties and clinical applications. *Journal of dentistry* **2007,** *35* (11), 819-826.
65. Kong, L.; Chen, W.; Ma, D.; Yang, Y.; Liu, S.; Huang, S., Size control of Au@ Cu 2 O octahedra for excellent photocatalytic performance. *J. Mater. Chem.* **2012,** *22* (2), 719-724.
66. Zhang, H.; Ji, Z.; Xia, T.; Meng, H.; Low-Kam, C.; Liu, R.; Pokhrel, S.; Lin, S.; Wang, X.; Liao, Y.-P., Use of metal oxide nanoparticle band gap to develop a predictive paradigm for oxidative stress and acute pulmonary inflammation. *ACS Nano* **2012,** *6* (5), 4349-4368.
67. Zhang, T.; Zhao, H.; He, S.; Liu, K.; Liu, H.; Yin, Y.; Gao, C., Unconventional route to encapsulated ultrasmall gold nanoparticles for high-temperature catalysis. *ACS Nano* **2014,** *8* (7), 7297-7304.
68. Natelson, D., *Nanostructures and Nanotechnology*. Cambridge University Press: 2015.
69. Zhang, J.; Tang, Y.; Lee, K.; Ouyang, M., Nonepitaxial growth of hybrid core-shell nanostructures with large lattice mismatches. *Science* **2010,** *327* (5973), 1634-1638.
70. Sun, H.; He, J.; Wang, J.; Zhang, S.-Y.; Liu, C.; Sritharan, T.; Mhaisalkar, S.; Han, M.-Y.; Wang, D.; Chen, H., Investigating the multiple roles of polyvinylpyrrolidone for a general methodology of oxide encapsulation. *J. Am. Chem. Soc.* **2013,** *135* (24), 9099-9110.
71. Zheleva, T.; Jagannadham, K.; Narayan, J., Epitaxial growth in large-lattice-mismatch systems. *J. Appl. Phys.* **1994,** *75* (2), 860-871.

72. Chen, Y.; Washburn, J., Structural transition in large-lattice-mismatch heteroepitaxy. *Phys. Rev. Lett.* **1996,** *77* (19), 4046.
73. Kukta, R.; Freund, L., Minimum energy configuration of epitaxial material clusters on a lattice-mismatched substrate. *Journal of the Mechanics and Physics of Solids* **1997,** *45* (11), 1835-1860.
74. Chen, Y.; Zhu, B.; Yao, M.; Wang, S.; Zhang, S., The preparation and characterization of Au@ TiO 2 nanoparticles and their catalytic activity for CO oxidation. *Catal. Commun.* **2010,** *11* (12), 1003-1007.
75. Qi, J.; Chen, J.; Li, G.; Li, S.; Gao, Y.; Tang, Z., Facile synthesis of core–shell Au@ CeO 2 nanocomposites with remarkably enhanced catalytic activity for CO oxidation. *Energy Environ. Sci.* **2012,** *5* (10), 8937-8941.
76. Liu, D.-Y.; Ding, S.-Y.; Lin, H.-X.; Liu, B.-J.; Ye, Z.-Z.; Fan, F.-R.; Ren, B.; Tian, Z.-Q., Distinctive enhanced and tunable plasmon resonant absorption from controllable Au@ Cu2O nanoparticles: experimental and theoretical modeling. *J. Phys. Chem. C* **2012,** *116* (7), 4477-4483.
77. Meir, N.; Jen-La Plante, I.; Flomin, K.; Chockler, E.; Moshofsky, B.; Diab, M.; Volokh, M.; Mokari, T., Studying the chemical, optical and catalytic properties of noble metal (Pt, Pd, Ag, Au)–Cu 2 O core–shell nanostructures grown via a general approach. *J. Mater. Chem. A* **2013,** *1* (5), 1763-1769.
78. Wang, W.-C.; Lyu, L.-M.; Huang, M. H., Investigation of the effects of polyhedral gold nanocrystal morphology and facets on the formation of Au–Cu2O core–shell heterostructures. *Chem. Mater.* **2011,** *23* (10), 2677-2684.
79. Zhang, L.; Blom, D. A.; Wang, H., Au–Cu2O core–shell nanoparticles: a hybrid metal-semiconductor heteronanostructure with geometrically tunable optical properties. *Chem. Mater.* **2011,** *23* (20), 4587-4598.
80. Lin, M.; Wang, Y.; Sun, X.; Wang, W.; Chen, L., “Elastic” Property of Mesoporous Silica Shell: For Dynamic Surface Enhanced Raman Scattering Ability Monitoring of Growing Noble Metal Nanostructures via a Simplified Spatially Confined Growth Method. *ACS Appl. Mater. Interfaces* **2015,** *7* (14), 7516-7525.
81. Chung, F.-C.; Wu, R.-J.; Cheng, F.-C., Fabrication of a Au@ SnO 2 core–shell structure for gaseous formaldehyde sensing at room temperature. *Sensors and Actuators B: Chemical* **2014,** *190*, 1-7.
82. Wu, R.-J.; Lin, D.-J.; Yu, M.-R.; Chen, M. H.; Lai, H.-F., Ag@ SnO 2 core–shell material for use in fast-response ethanol sensor at room operating temperature. *Sensors and Actuators B: Chemical* **2013,** *178*, 185-191.
83. Goebl, J.; Joo, J. B.; Dahl, M.; Yin, Y., Synthesis of tailored Au@ TiO 2 core–shell nanoparticles for photocatalytic reforming of ethanol. *Catal. Today* **2014,** *225*, 90-95.
84. Fang, C.; Jia, H.; Chang, S.; Ruan, Q.; Wang, P.; Chen, T.; Wang, J., (Gold core)/(titania shell) nanostructures for plasmon-enhanced photon harvesting and generation of reactive oxygen species. *Energy Environ. Sci.* **2014,** *7* (10), 3431-3438.

85. Bond, G. C., Gold: a relatively new catalyst. *Catal. Today* **2002,** *72* (1), 5-9.
86. Ge, J.; Zhang, Q.; Zhang, T.; Yin, Y., Core–satellite nanocomposite catalysts protected by a porous silica shell: controllable reactivity, high stability, and magnetic recyclability. *Angew. Chem.* **2008,** *120* (46), 9056-9060.
87. Poovarodom, S.; Bass, J. D.; Hwang, S.-J.; Katz, A., Investigation of the Core−Shell Interface in Gold@Silica Nanoparticles: A Silica Imprinting Approach. *Langmuir* **2005,** *21* (26), 12348-12356.
88. Liz-Marzán, L. M.; Giersig, M.; Mulvaney, P., Synthesis of Nanosized Gold−Silica Core−Shell Particles. *Langmuir* **1996,** *12* (18), 4329-4335.
89. Zhang, J.; Li, L.; Huang, X.; Li, G., Fabrication of Ag–CeO 2 core–shell nanospheres with enhanced catalytic performance due to strengthening of the interfacial interactions. *J. Mater. Chem.* **2012,** *22* (21), 10480-10487.
90. Zhang, N.; Xu, Y.-J., Aggregation-and leaching-resistant, reusable, and multifunctional Pd@ CeO2 as a robust nanocatalyst achieved by a hollow core–shell strategy. *Chem. Mater.* **2013,** *25* (9), 1979-1988.
91. Tsuji, M.; Matsuo, R.; Jiang, P.; Miyamae, N.; Ueyama, D.; Nishio, M.; Hikino, S.; Kumagae, H.; Kamarudin, K. S. N.; Tang, X.-L., Shape-dependent evolution of Au@ Ag core− shell nanocrystals by PVP-assisted N, N-dimethylformamide reduction. *Crystal Growth and Design* **2008,** *8* (7), 2528-2536.
92. Arnal, P. M.; Comotti, M.; Schüth, F., High-Temperature-Stable Catalysts by Hollow Sphere Encapsulation. *Angew. Chem.* **2006,** *118* (48), 8404-8407.
93. Qu, Y.; Liu, F.; Wei, Y.; Gu, C.; Zhang, L.; Liu, Y., Forming ceria shell on Au-core by LSPR photothermal induced interface reaction. *Appl. Surf. Sci.* **2015,** *343*, 207-211.
94. Li, B.; Gu, T.; Ming, T.; Wang, J.; Wang, P.; Wang, J.; Yu, J. C., (Gold core)@(ceria shell) nanostructures for plasmon-enhanced catalytic reactions under visible light. *ACS Nano* **2014,** *8* (8), 8152-8162.
95. Han, L.; Zhu, C.; Hu, P.; Dong, S., One-pot synthesis of a Au@ TiO 2 core–shell nanocomposite and its catalytic property. *RSC Adv.* **2013,** *3* (31), 12568-12570.
96. Han, L.; Wei, H.; Tu, B.; Zhao, D., A facile one-pot synthesis of uniform core–shell silver nanoparticle@ mesoporous silica nanospheres. *Chem. Commun.* **2011,** *47* (30), 8536-8538.
97. Jiang, W.; Zhou, Y.; Zhang, Y.; Xuan, S.; Gong, X., Superparamagnetic Ag@ Fe 3 O 4 core–shell nanospheres: fabrication, characterization and application as reusable nanocatalysts. *Dalton Trans.* **2012,** *41* (15), 4594-4601.
98. Güttel, R.; Paul, M.; Galeano, C.; Schüth, F., Au,@ ZrO 2 yolk–shell catalysts for CO oxidation: Study of particle size effect by ex-post size control of Au cores. *J. Catal.* **2012,** *289*, 100-104.
99. Bauer, J. C.; Toops, T. J.; Oyola, Y.; Parks II, J. E.; Dai, S.; Overbury, S. H., Catalytic activity and thermal stability of Au–CuO/SiO 2 catalysts for the low

temperature oxidation of CO in the presence of propylene and NO. *Catal. Today* **2014,** *231*, 15-21.
100. dell'Erba, I. E.; Hoppe, C. E.; Williams, R. J. J., Films of covalently bonded gold nanoparticles synthesized by a sol–gel process. *Journal of Nanoparticle Research* **2012,** *14* (9), 1-8.
101. Mamyrin, B., Laser assisted reflectron time-of-flight mass spectrometry. *Int. J. Mass Spectrom. Ion Processes* **1994,** *131*, 1-19.
102. Kothalawala, N.; Kumara, C.; Ferrando, R.; Dass, A., Au 144− x Pd x (SR) 60 nanomolecules. *Chem. Commun.* **2013,** *49* (92), 10850-10852.
103. Dass, A.; Stevenson, A.; Dubay, G. R.; Tracy, J. B.; Murray, R. W., Nanoparticle MALDI-TOF mass spectrometry without fragmentation: Au25 (SCH2CH2Ph) 18 and mixed monolayer Au25 (SCH2CH2Ph) 18− x (L) x. *J. Am. Chem. Soc.* **2008,** *130* (18), 5940-5946.
104. Thomas, S.; Shanks, R.; Chandran, S., *Nanostructured polymer blends*. William Andrew: 2013.
105. Gürsoy, M.; Karaman, M., *Surface Treatments for Biological, Chemical and Physical Applications*. John Wiley & Sons: 2017.
106. Andor Atomic Spectroscopy. http://www.andor.com/learning-academy/atomic-spectroscopy-atomic-absorption,-emission-and-fluorescence-techniques.
107. Hodnett, B. K., *Heterogeneous catalytic oxidation: fundamental and technological aspects of the selective and total oxidation of organic compounds*. Wiley: 2000.
108. Nellist, P. D.; Pennycook, S. J., *Scanning Transmission Electron Microscopy: Imaging and Analysis*. Springer: 2011.
109. Van der Heide, P., *X-ray photoelectron spectroscopy: an introduction to principles and practices*. John Wiley & Sons: 2011.
110. Foo, G. S.; Polo Garzon, F.; Fung, V.; Jiang, D.-e.; Overbury, S. H.; Wu, Z., Acid-Base Reactivity of Perovskite Catalysts Probed via Conversion of 2-Propanol over Titanates and Zirconates. *ACS Catalysis* **2017**.
111. Wojcieszak, R.; Genet, M.; Eloy, P.; Ruiz, P.; Gaigneaux, E., Determination of the size of supported Pd nanoparticles by X-ray photoelectron spectroscopy. Comparison with X-ray diffraction, transmission electron microscopy, and H2 chemisorption methods. *J. Phys. Chem. C* **2010,** *114* (39), 16677-16684.
112. Wu, Z.; Jiang, D.-e.; Mann, A. K.; Mullins, D. R.; Qiao, Z.-A.; Allard, L. F.; Zeng, C.; Jin, R.; Overbury, S. H., Thiolate ligands as a double-edged sword for CO oxidation on CeO2 supported Au25 (SCH2CH2Ph) 18 nanoclusters. *J. Am. Chem. Soc.* **2014,** *136* (16), 6111-6122.
113. Wu, Z.; Zhou, S.; Zhu, H.; Dai, S.; Overbury, S. H., DRIFTS-QMS study of room temperature CO oxidation on Au/SiO2 catalyst: Nature and role of different Au species. *J. Phys. Chem. C* **2009,** *113* (9), 3726-3734.

APPENDIX

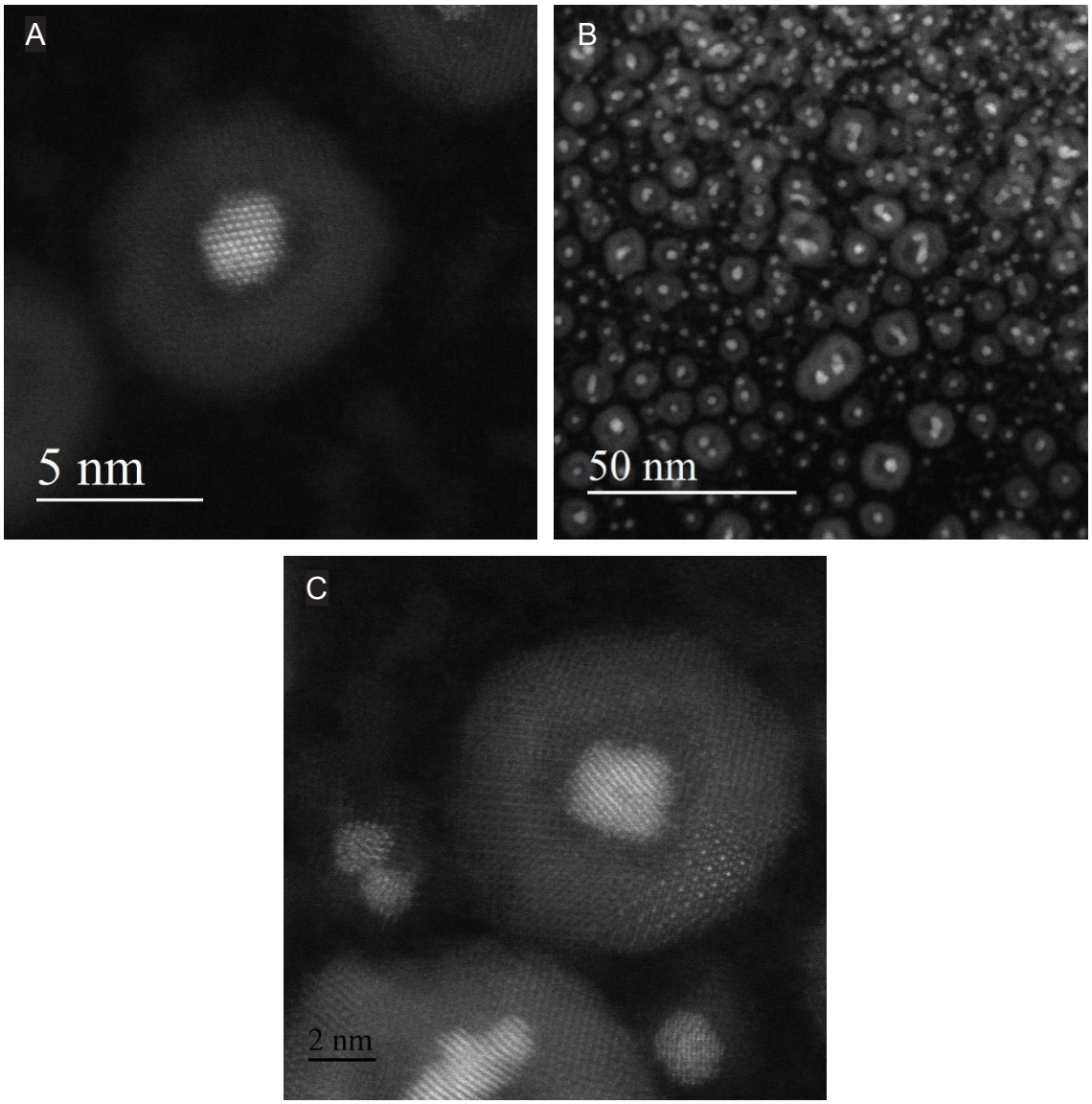

Figure 34. A, B, & C) HAADF-STEM of $Au_{144}@Fe_2O_3$ 1:4 structure, pre-calcined.

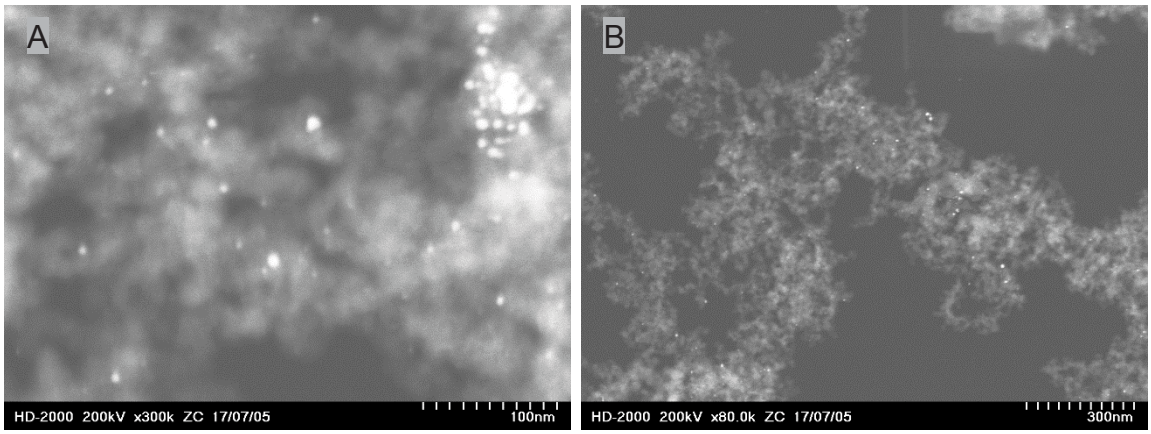

Figure 35. A & B) STEM of $Au_{144}@Fe_2O_3/SiO_2$ 1:2 structure, calcined at 300 °C.

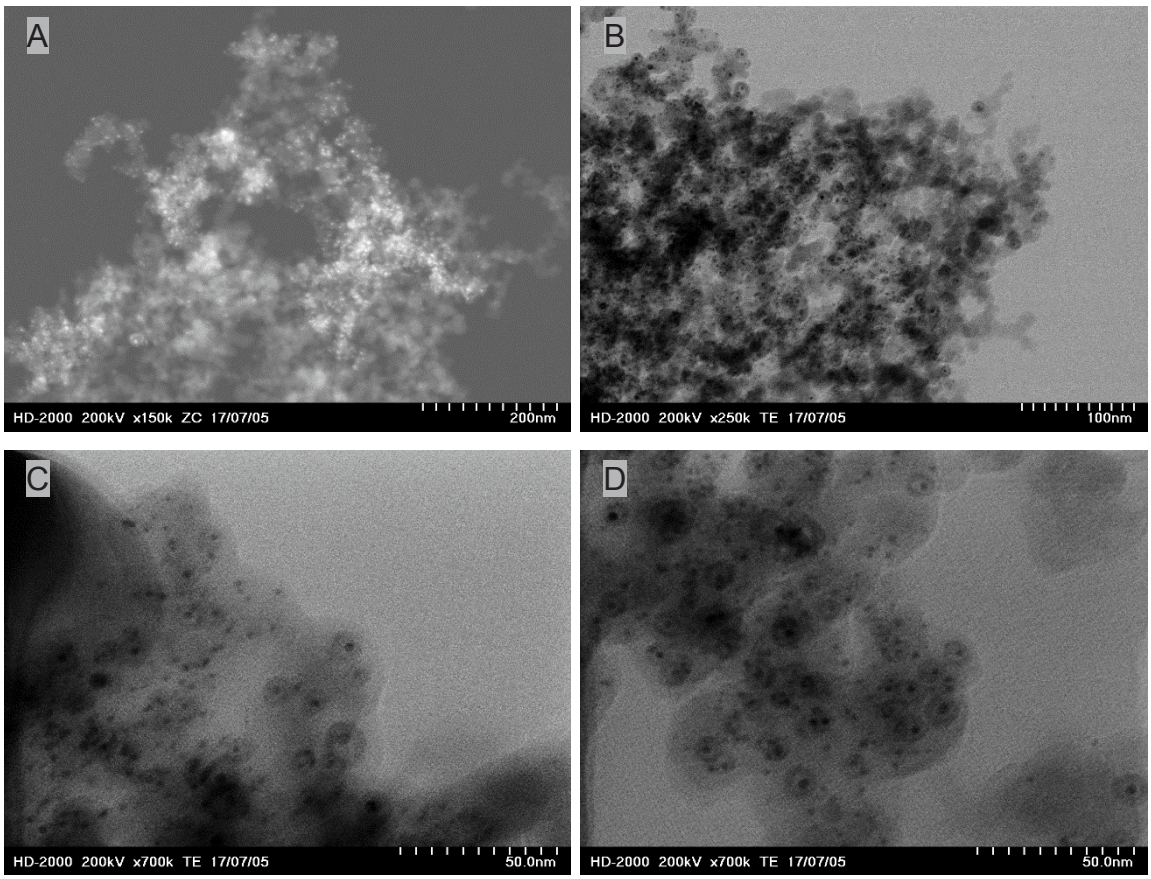

Figure 36. A-D) STEM of $Au_{144}@Fe_2O_3/SiO_2$ 1:4 structure, calcined at 300 °C.

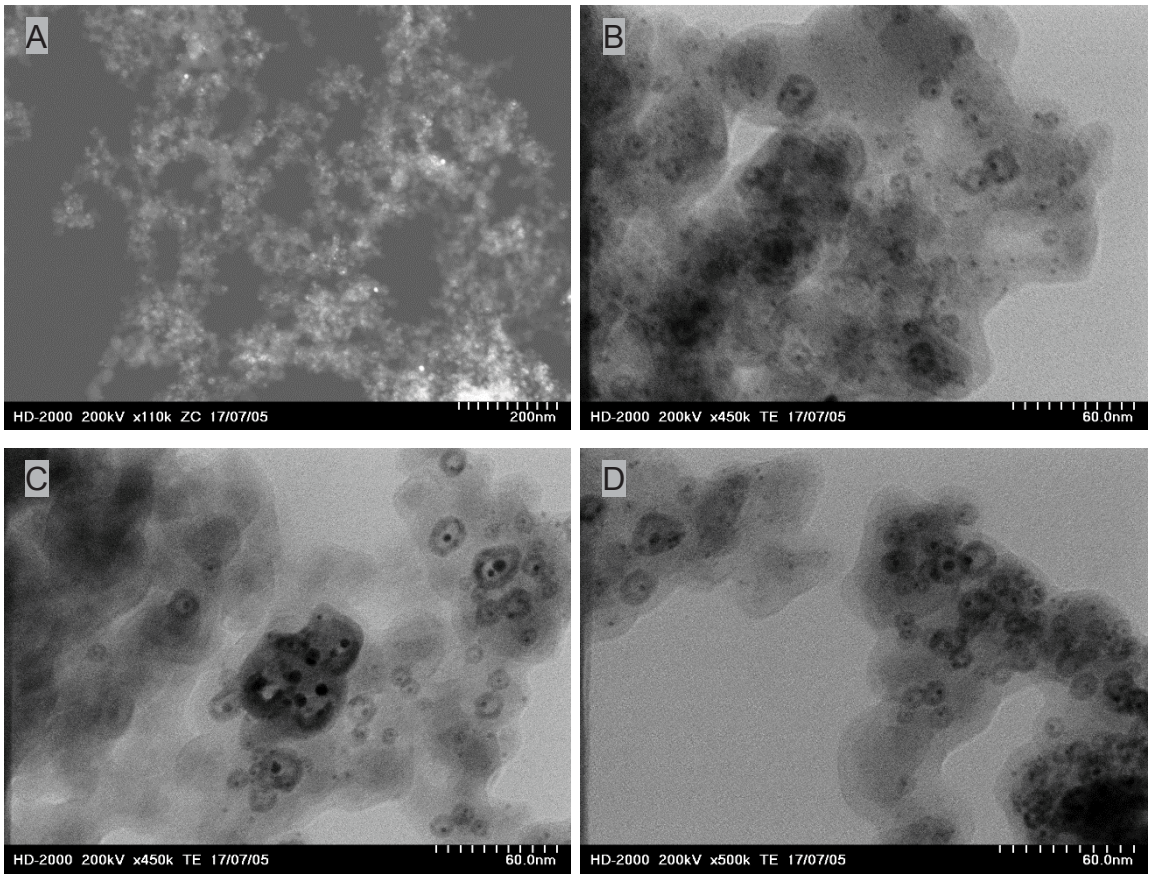

Figure 37. A-D) STEM of $Au_{144}@Fe_2O_3/SiO_2$ 1:6 structure, calcined at 300 °C.

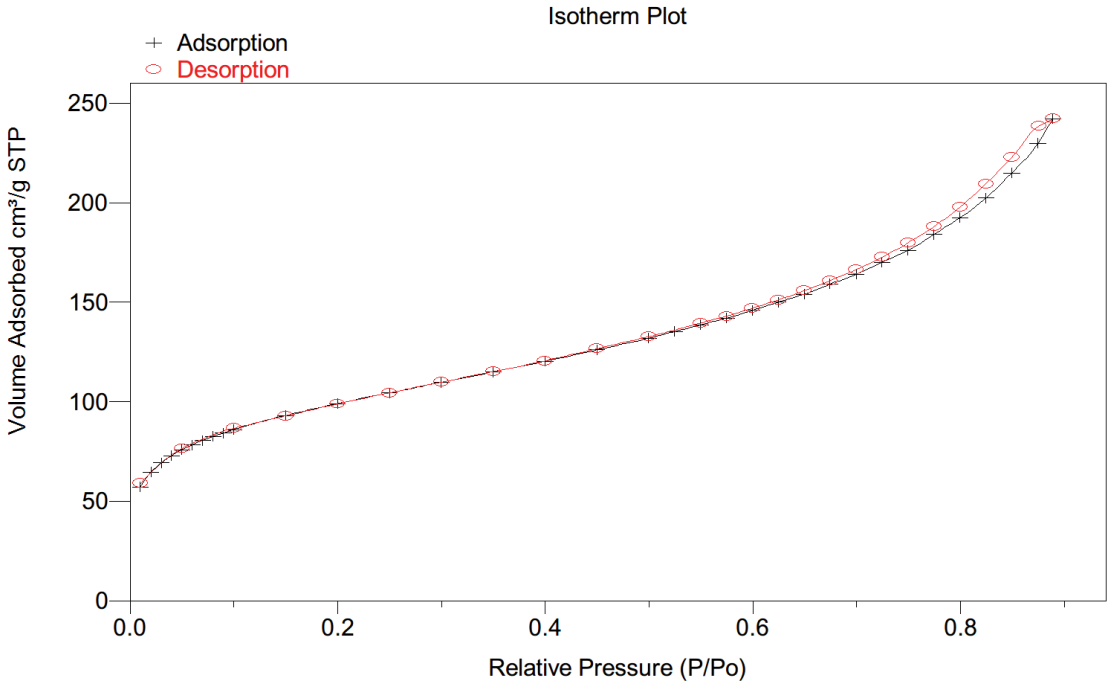

Figure 38. Isotherm for adsorption-desorption of N_2 at 77 K on fumed silica (SiO_2).

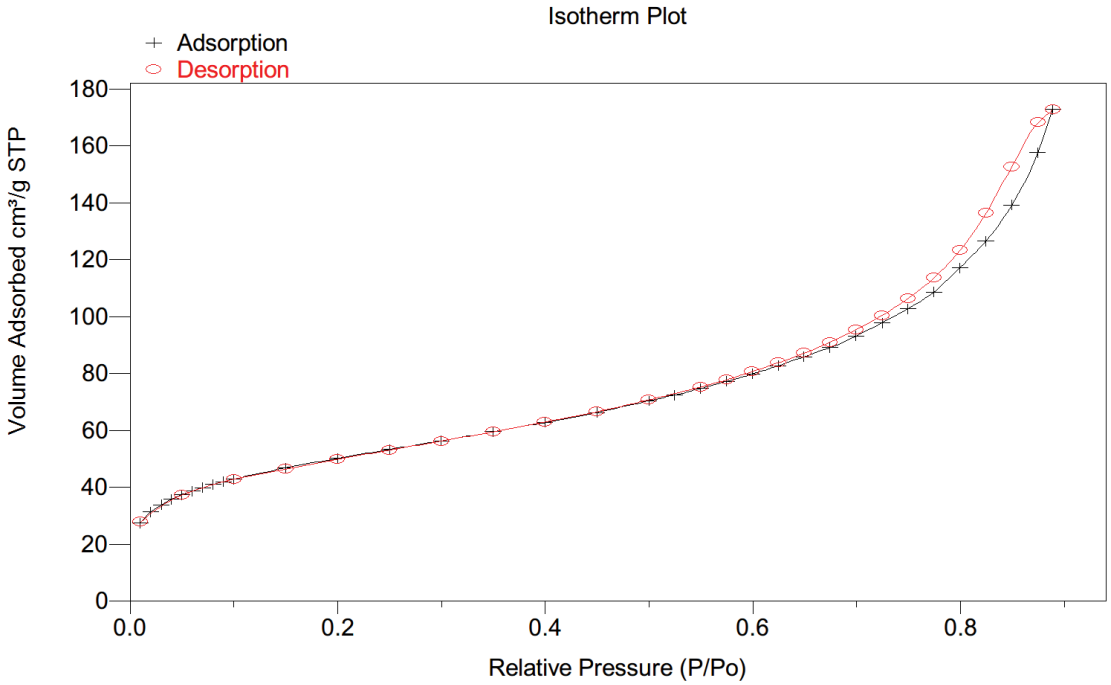

Figure 39. Isotherm for adsorption-desorption of N_2 at 77 K on Fe_2O_3/SiO_2 with 2.3% Fe loading.

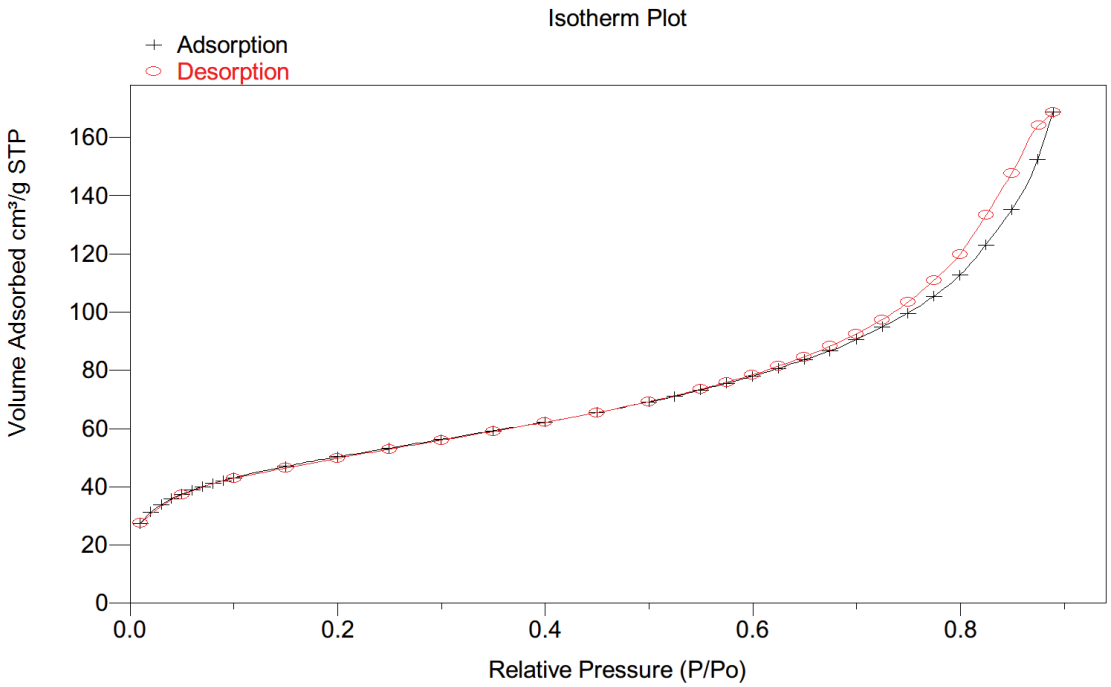

Figure 40. Isotherm for adsorption-desorption of N_2 at 77 K on Au_{144}/SiO_2 with 1.4% Au loading.

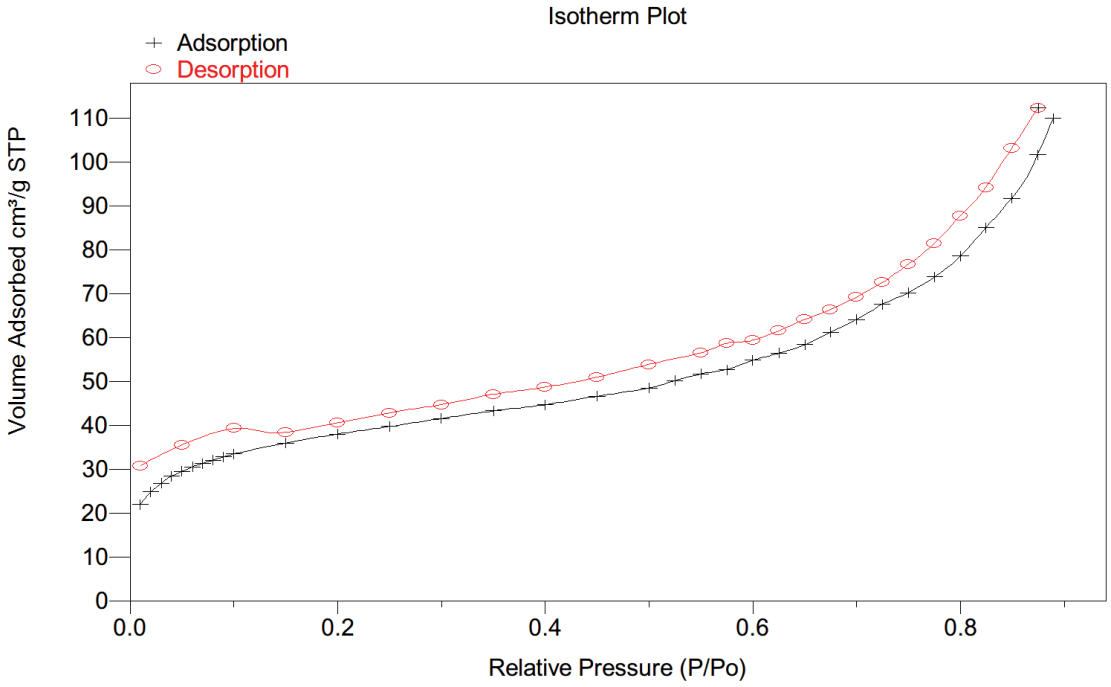

Figure 41. Isotherm for adsorption-desorption of N_2 at 77 K on 1:2 Au:Fe by mass $Au_{144}@Fe_2O_3/SiO_2$ with 1.2% Au loading.

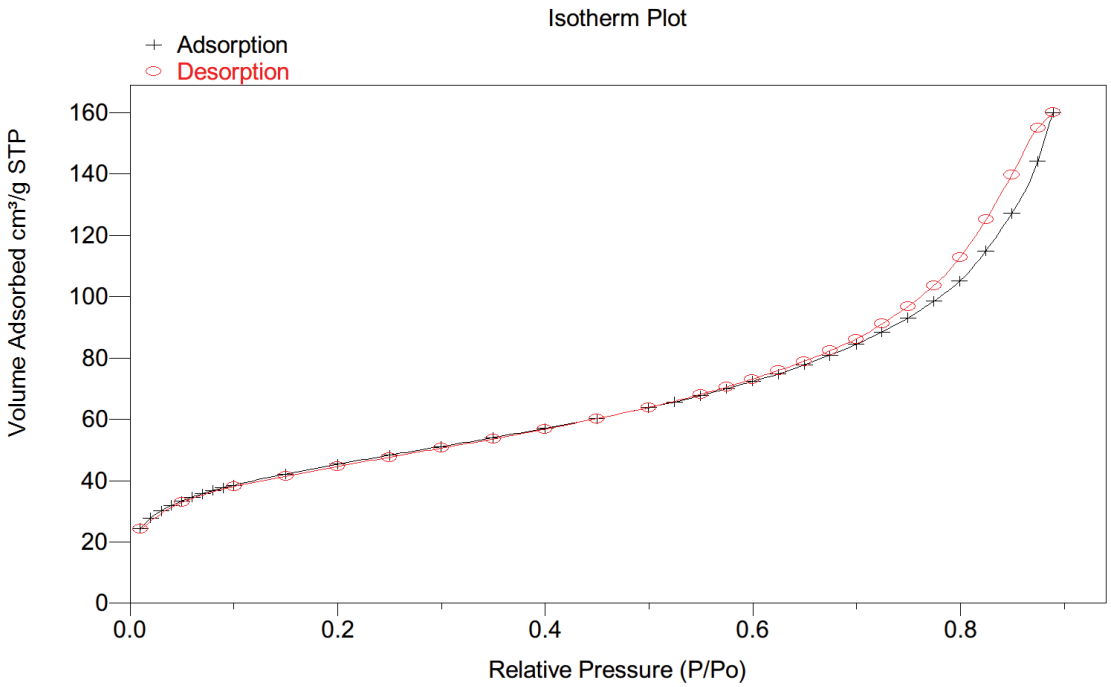

Figure 42. Isotherm for adsorption-desorption of N_2 at 77 K on 1:4 Au:Fe by mass Au_{144}@Fe_2O_3/SiO_2 with 1.7% Au loading.

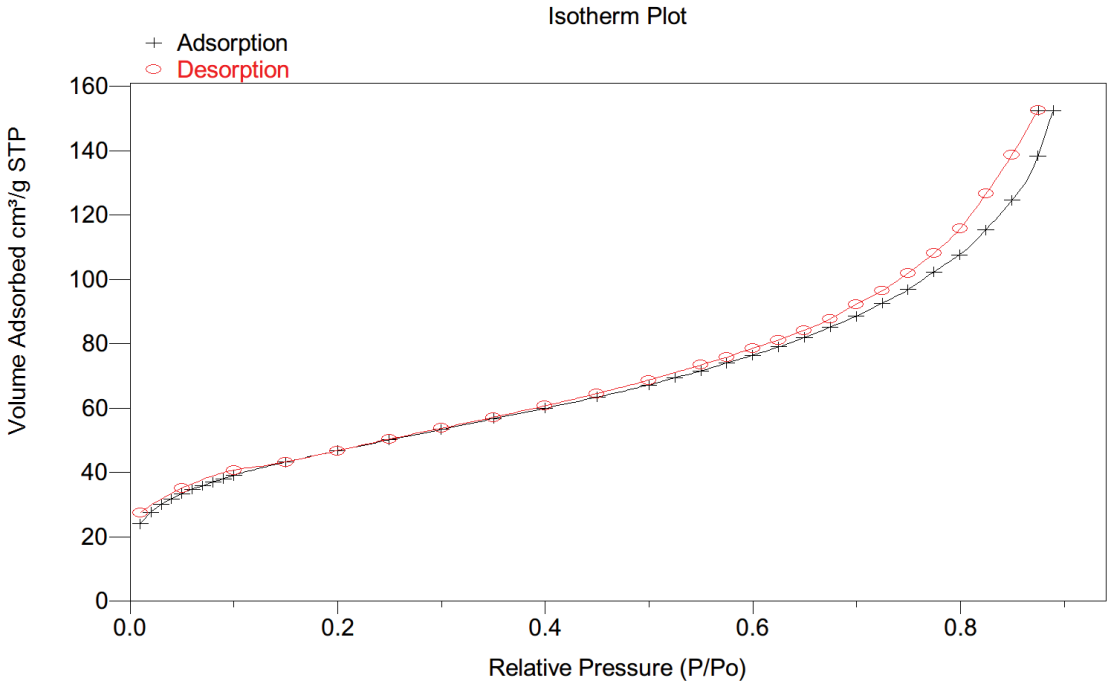

Figure 43. Isotherm for adsorption-desorption of N_2 at 77 K on 1:6 Au:Fe by mass Au_{144}@Fe_2O_3/SiO_2 with 1.5% Au loading.

VITA

Michelle E. Lukosi was born and raised in Kansas City, MO as the second child of ten. After high school, she obtained a B.A. in International Business from Benedictine College, and got engaged and married the love of her life, Eric Lukosi. After attaining her B.A. degree she proceeded to work a few different jobs, with tasks including data entry and non-certified accounting for Missouri Jiffy Lube stores before she decided that she needed something different. She subsequently joined the United States Air Force Reserves as a Bioenvironmental Engineer. During her time in the Air Force, she earned a B.S. in Chemistry from the University of Missouri. Subsequently, she was accepted into the Chemistry graduate program at the University of Tennessee. During her graduate career, she brought into the world her two beautiful children, Aria and Ian, while also studying and synthesizing novel gold cluster-metal oxide core-shell catalytic systems.